SUPPLEMENTARY ONLINE MATERIAL

High-Performance Hybrid Biofuel Cells Using Amphiphilic Assembly-Based Enzyme Electrodes

Cheong Hoon Kwon[1], Minchul Kang[1], Minseong Kwon[1], Donghyeon Nam[1], Yongkwon Song [1], Euiju Yong[1], Min-Kyu Oh[1], Yongju Kim[2], Bongjun Yeom[3], Jun Hyuk Moon[4], Seung Woo Lee[5,a], and Jinhan Cho[1,2,b]

AFFILIATIONS

[1]Department of Chemical & Biological Engineering, Korea University, 145 Anam-ro, Seongbuk-gu, Seoul 02841, Republic of Korea

[2]KU-KIST Graduate School of Converging Science and Technology, Korea University, 145 Anam-ro, Seongbuk-gu, Seoul 02841, Republic of Korea

[3]Department of Chemical Engineering, Hanyang University, 222 Wangsimni-ro, Seongdong-gu, Seoul 04763, Republic of Korea

[4]Department of Chemical and Biomolecular Engineering, Sogang University, Baekbeom-ro 35, Mapo-gu, Seoul 04107, Republic of Korea
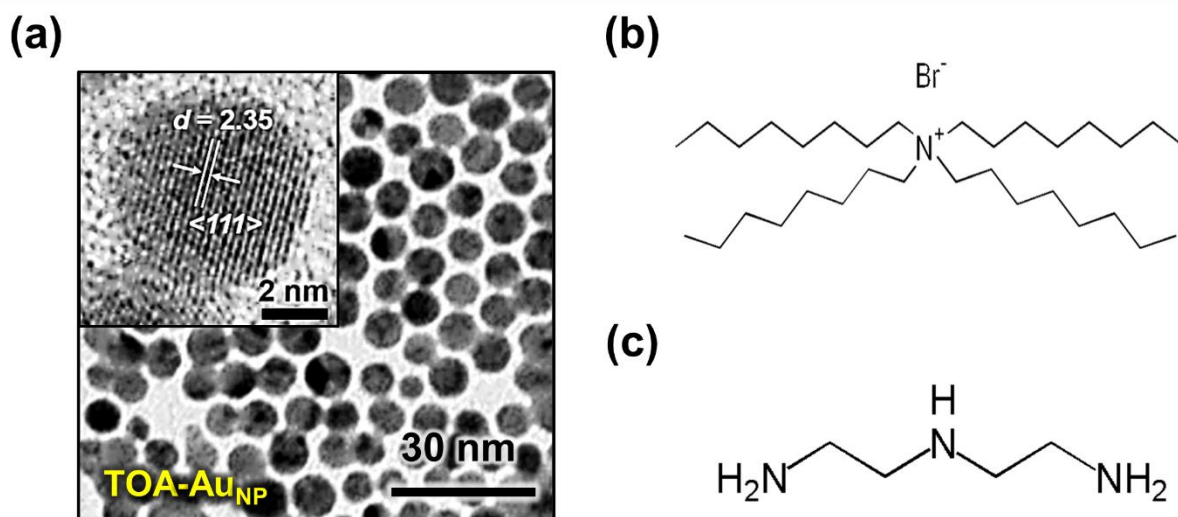
[5]The George W. Woodruff School of Mechanical Engineering, Georgia Institute of Technology Atlanta, GA 30332, USA

Author to whom correspondence should be addressed: [a]seung.lee@me.gatech.edu, [b]jinhan71@korea.ac.kr
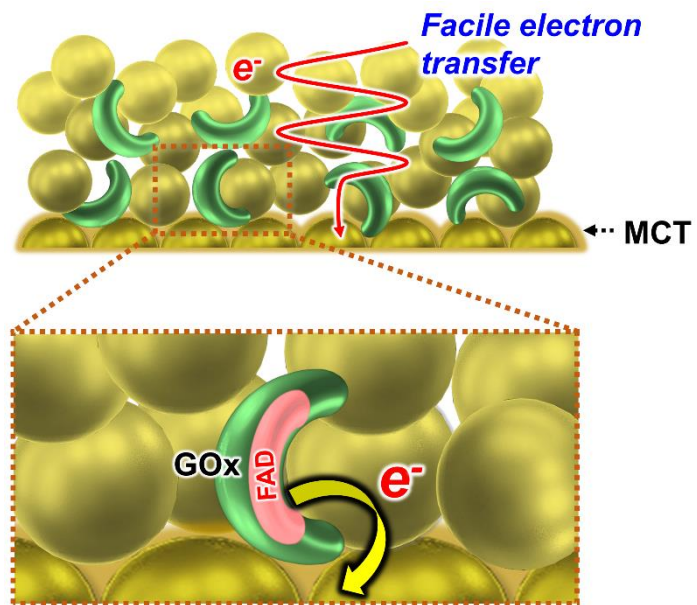
FIG. S1. The electron transfer distance between the FAD center of GOx and electrodes on the highly porous MCT electrode.

FIG. S2. TOA-Au$_{NPs}$ and ligands. (a) High-resolution transmission electron microscopy (HR-TEM) image of TOA-Au$_{NP}$ (6 ± 2 nm). The inset shows the spacing of the lattice fringe of the TOA-Au$_{NP}$ (2.4 Å), which corresponds to the Au (111) crystalline planes. The molecular structures of (b) native TOA ligand and (c) amine-functionalized diethylenetriamine (DETA). In this case, TOA ligands with ammonium groups are loosely bound to the surface of Au NPs. On the other hand, the DETA linkers contain primary (-NH$_2$) and secondary amine (-NH-) groups having a higher affinity (i.e., coordination-bonding interaction) for Au$_{NPs}$ compared to the ammonium ion-containing TOA ligands.[S1] Therefore, when DETA linkers are adsorbed onto TOA-Au$_{NPs}$ layer, the primary and secondary amine groups of DETA can be directly adsorbed onto the surface of Au$_{NPs}$ through ligand exchange reaction between bulky TOA ligands and DETA linkers.
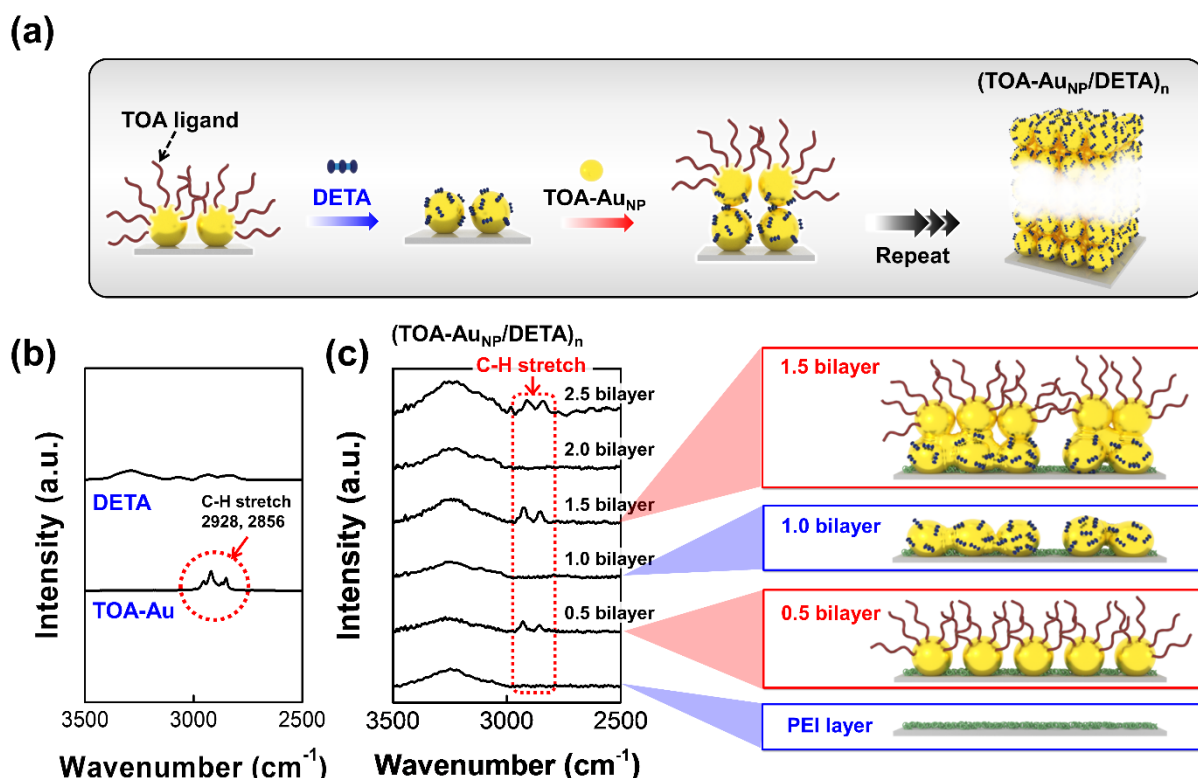
FIG. S3. Ligand exchange reaction. (a) Schematic representation of (TOA-Au$_{NP}$/DETA)$_n$ multilayers using ligand exchange reaction-induced LbL assembly. (b) FTIR spectra of TOA-Au$_{NP}$ and DETA. In the case of TOA-Au$_{NP}$, the notable absorbance peaks at 2928 and 2856 cm^{-1} originated from the C–H stretching of TOA ligands with long alkyl chains, which were traced to investigate the ligand replacement reaction between the TOA ligands bound to Au$_{NP}$ surface and the NH$_2$ groups of DETA during repetitive LbL deposition. (c) FTIR spectra and schematic representation of ligand-exchange reaction-induced LbL-assembled (TOA-Au$_{NP}$/DETA)$_n$ multilayers onto the PEI-coated Si wafer. Specifically, the first deposition of TOA-Au$_{NP}$ onto the NH$_2$-functionalized Si wafer (i.e., n=0.5 bilayer) exhibited the characteristic C—H stretching peaks (at 2928 and 2856 cm^{-1}) by long alkyl chains of bulky TOA ligands. However, the subsequent adsorption of DETA linkers onto the outermost TOA-Au$_{NP}$ layer (i.e., n=1 bilayer) eliminated the C—H stretching peaks of TOA ligands. These ligand exchange reactions were sequentially repeated during LbL assembly.
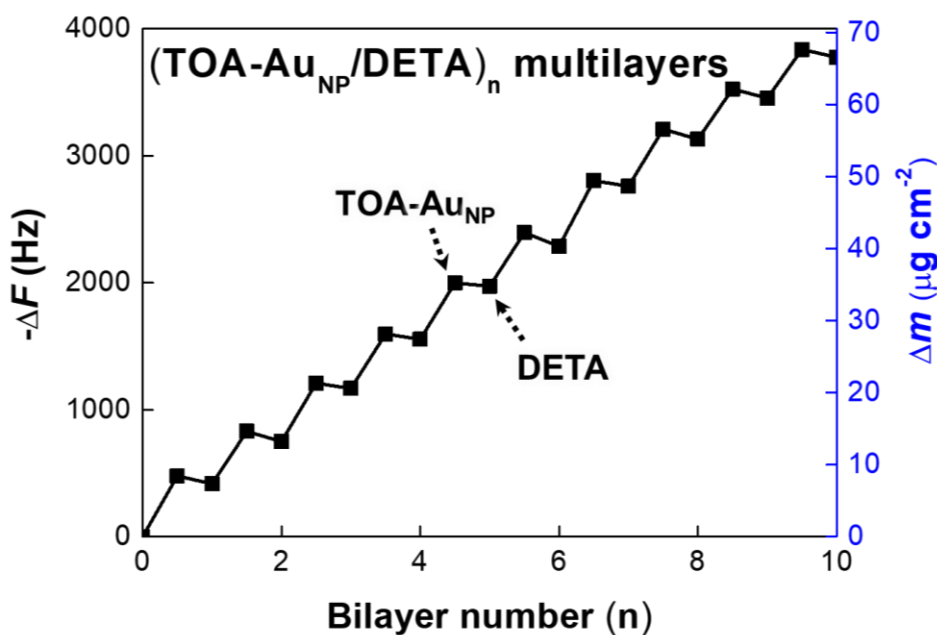
FIG. S4. QCM analysis. Frequency ($-\Delta F$) and mass changes (Δm) of (TOA-Au$_{NP}$/DETA)$_n$ multilayers as a function of the number of bilayers (n) using QCM analysis. The mass changes per layer were calculated from the frequency changes of the TOA-Au$_{NP}$ and the DETA layers adsorbed on the QCM electrode using a Sauerbrey equation. The total adsorbed amount of the (TOA-Au$_{NP}$ in toluene /DETA in ethanol)$_{10}$ multilayer was measured to be approximately 66.5 µg cm^{-2}. The slight decrease in the mass changes occurring during the deposition of DETA implied that the bulky TOA (M$_w$ ≈ 547) ligands was replaced by the extremely small DETA molecules (M$_w$ ≈ 103). In addition, the small molecule (DETA)-based LbL assembly in organic media could significantly decrease the separation distance between neighboring NPs, resulting in the formation of densely packed TOA-Au$_{NP}$ arrays with high electrical conductivity.
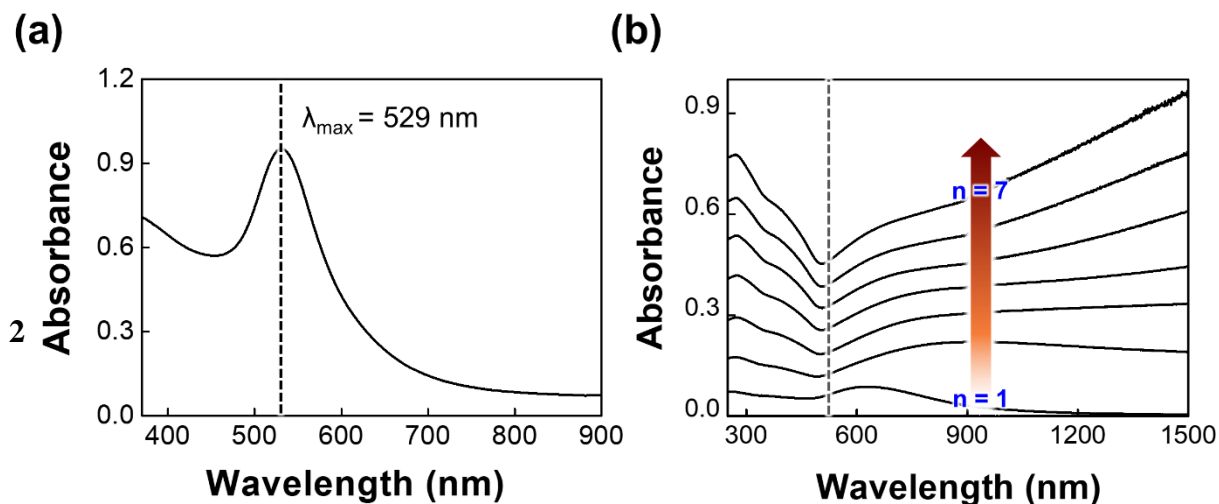
FIG. S5. Optical analysis. (a) UV absorbance spectrum of TOA-Au$_{NP}$ dispersed in toluene. (b) UV-vis absorbance spectra of (TOA-Au$_{NP}$/DETA)$_n$ multilayers assembled onto the quartz substrate as a function of bilayer number (n). Although the plasmon absorption peak (λ_{max}) of TOA-Au$_{NP}$ dispersed in toluene was located at 529 nm, the absorption peak of (TOA-Au$_{NP}$/DETA)$_n$ multilayers was gradually broadened and red shifted to the near-infrared (IR) region as the number of bilayers increased from 1 to 7. Considering that the surface plasmon resonance peak of Au$_{NP}$ is closely related to the NP–NP distance, these results suggest that the interparticle distance between the Au$_{NPs}$ was notably decreased in both the lateral and vertical dimensions.
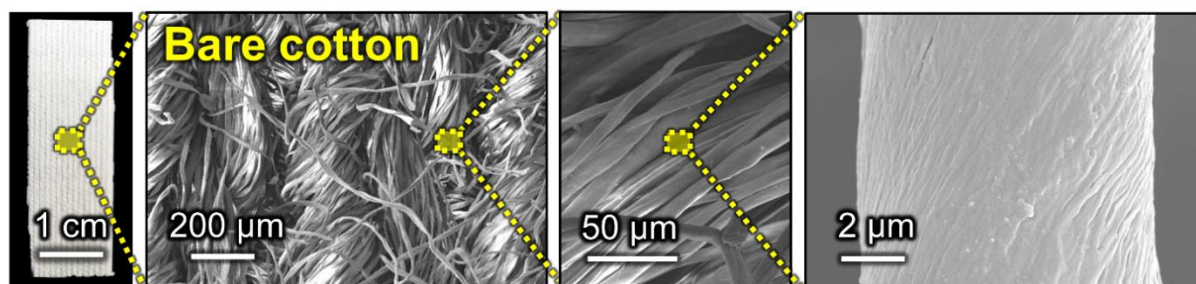
FIG. S6. Surface morphology. Field-emission scanning electron microscopy (FE-SEM) morphological images of bare cotton textile.
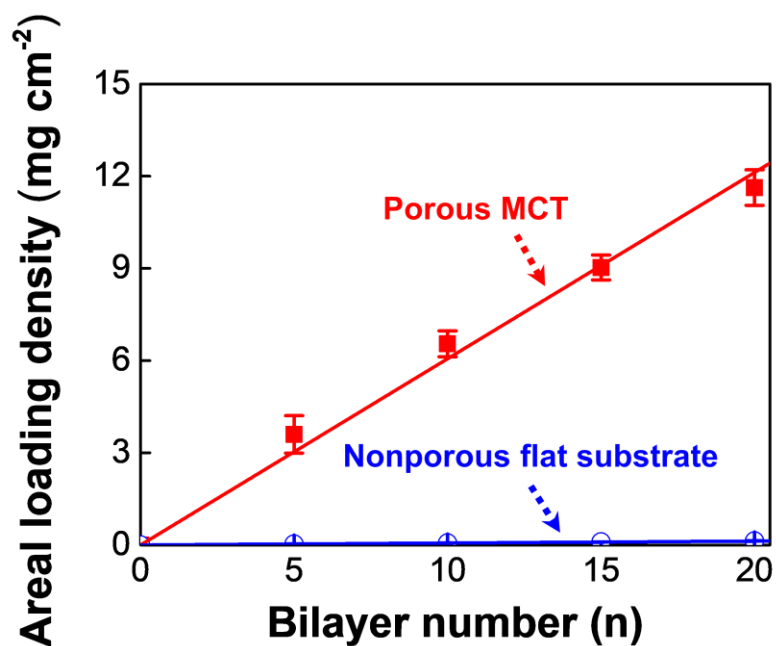
FIG. S7. Areal loading density. Change in the areal loading amount of the $(TOA-Au_{NP}/DETA)_n$ multilayers deposited onto porous MCT electrode and nonporous Au-coated QCM electrodes as a function of bilayer number (n). The loading amount of the $(TOA-Au_{NP}/DETA)_n$ multilayers adsorbed onto the cotton textile electrode was measured using an analytical balance.
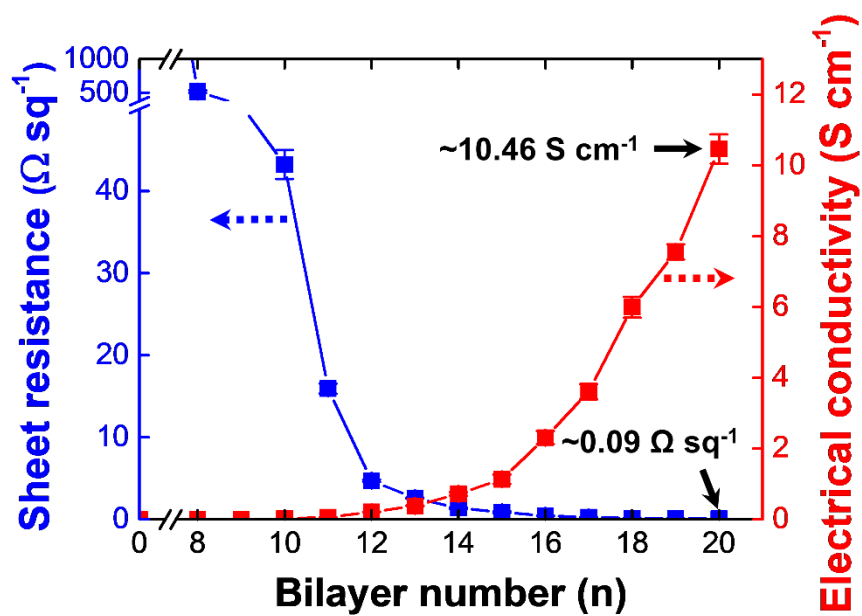
FIG. S8. Electrical properties. Sheet resistance and electrical conductivity of (TOA-Au$_{NP}$ /DETA)$_n$-coated cotton textile electrodes (i.e., n-MCTs) as a function of bilayer number (n).
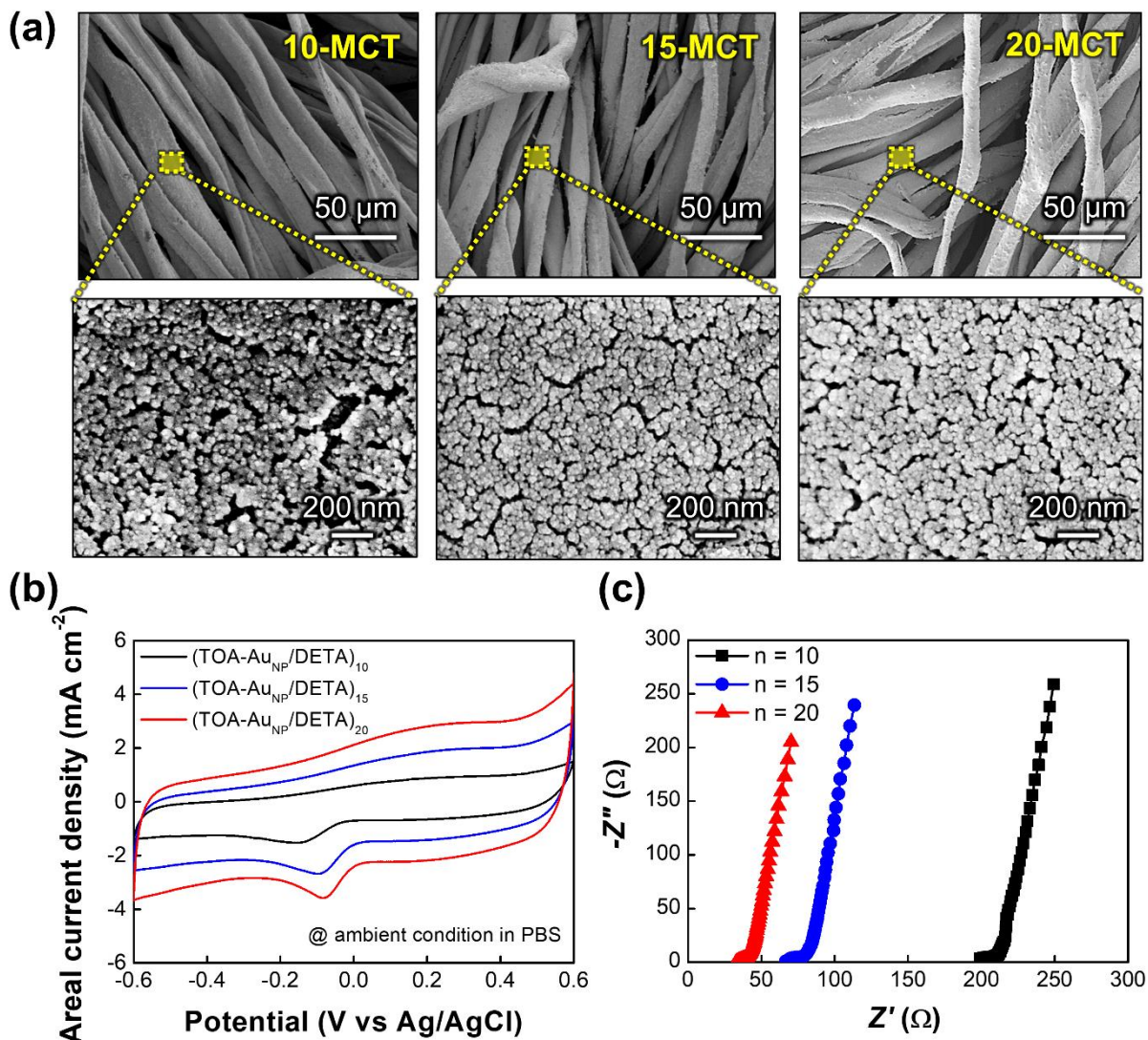
FIG. S9. Surface morphology and electrochemical performance. (a) FE-SEM images of n-MCT electrodes with increasing the bilayer number of (TOA-Au$_{NP}$/DETA)$_n$ multilayers (n = 10, 15, and 20). In this case, the LbL-assembled Au$_{NPs}$ were densely and homogeneously deposited onto the cotton textiles without notable NP agglomerations. (b) CV curves of n-MCT electrodes at a scan rate of 5 mV s^{-1} in PBS solution. (c) Nyquist plots of n-MCT in the frequency range 0.2 Hz to 100 kHz. These spectra composed of equivalent series resistance (ESR, including electrolyte resistance, contact resistance at materials/current collector interface, and intrinsic resistance of electrode materials) at high frequency region (intercept of *x*-axis), charge transfer resistance (R$_{ct}$) at middle frequency region (semicircular arch), and Warburg impedance (Z$_w$) at low frequency (linear tail). The ESR values at n = 10, 15, and 20 were measured to be approximately 209, 72, and 37 Ω, respectively. Additionally, the charge transfer resistance (*R$_{ct}$*) values were measured to be approximately 17 Ω for n=10, 14 Ω for n=15, and 9 Ω for n = 20, respectively.

10
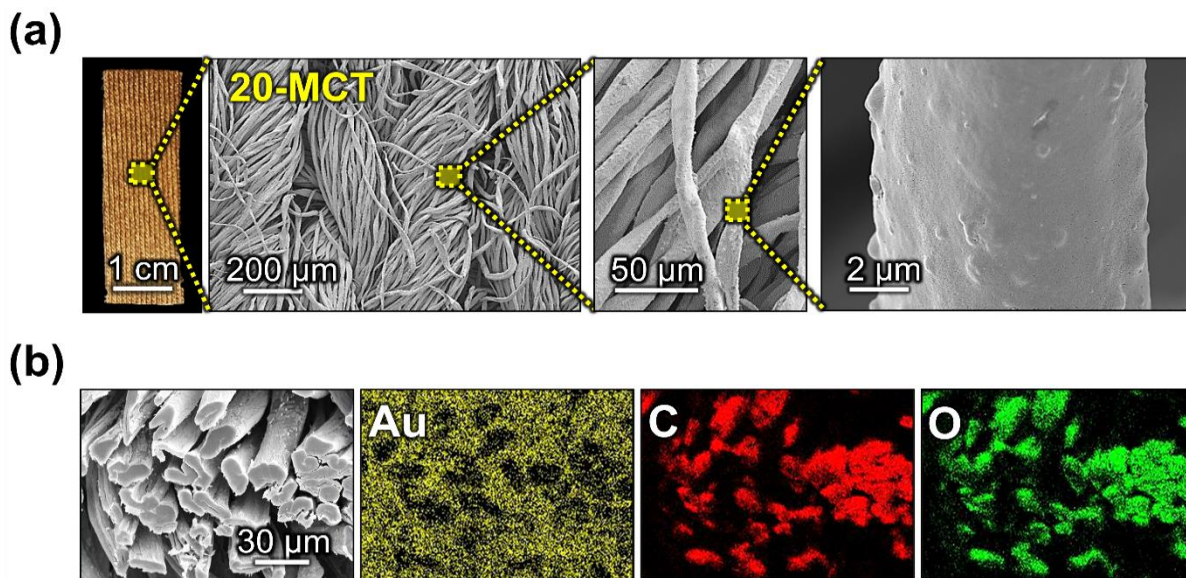
FIG. S10. Surface morphology and elemental analysis of MCT. (a) Photographic and planar FE-SEM images of 20-MCT (i.e., (TOA-Au$_{NP}$/DETA)$_{20}$ multilayer-coated cotton textile). (b) Cross-sectional FE-SEM and energy-dispersive X-ray spectroscopy (EDS) mapping images of the 20-MCT.
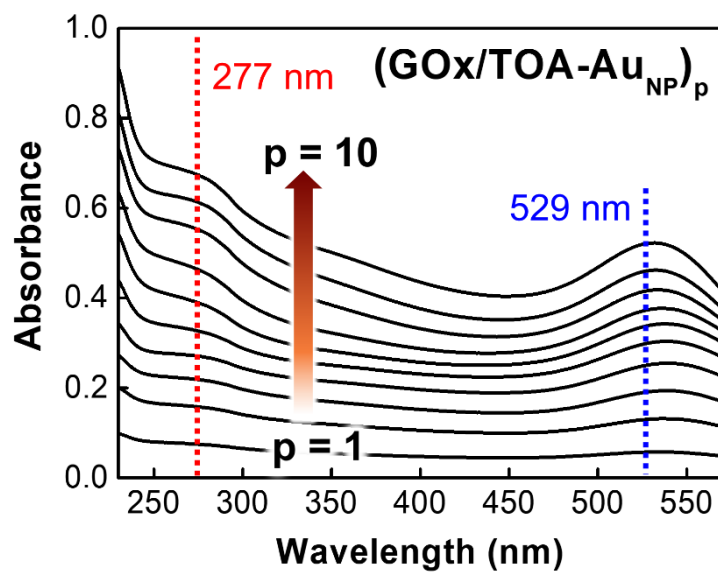
FIG. S11. Deposition mechanism analysis of (GOx/hydrophobic conductive metal NP)$_p$ multilayers. Ultraviolet-visible (UV-vis) absorbance spectra of (GOx/TOA-Au$_{NP}$)$_p$ multilayers on quartz glass. The prominent absorption peaks at 277 nm and 529 nm were associated with the oxidized flavin cofactor in GOx and TOA-Au$_{NP}$, respectively.
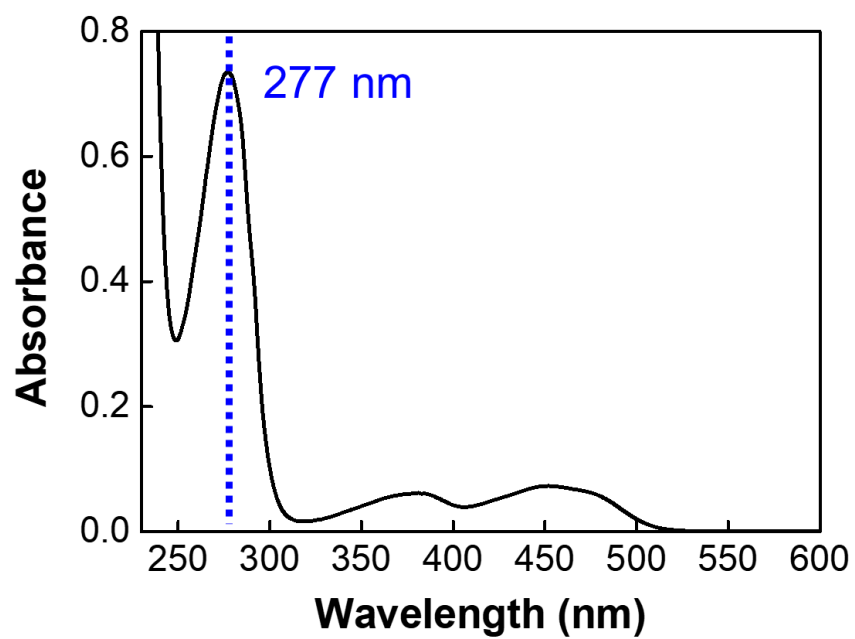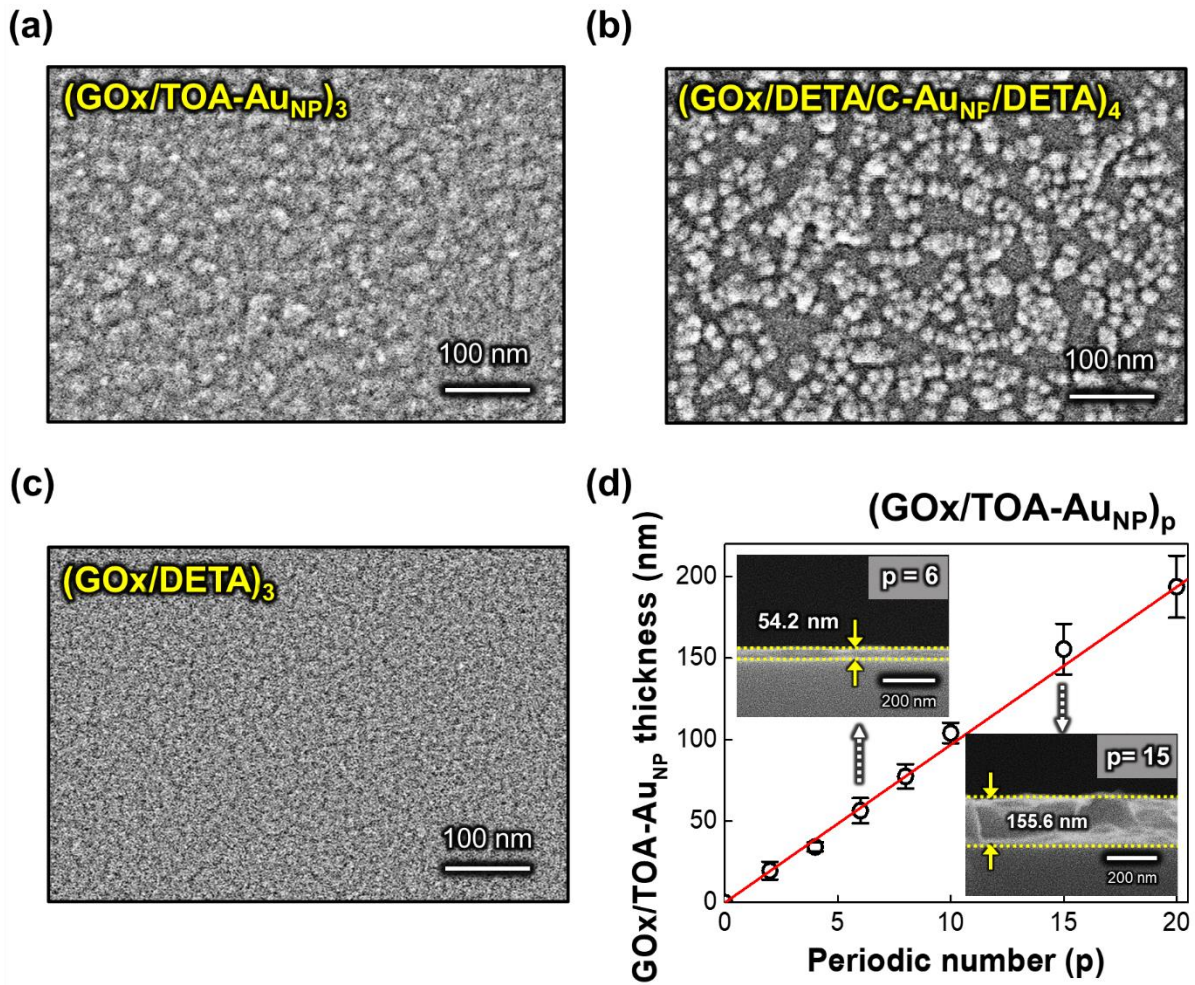
FIG. S12. UV-vis spectrum of GOx. UV-vis absorbance spectrum of GOx aqueous solution with a prominent absorption peak at 277 nm associated with the oxidized flavin cofactor in GOx.[S2]
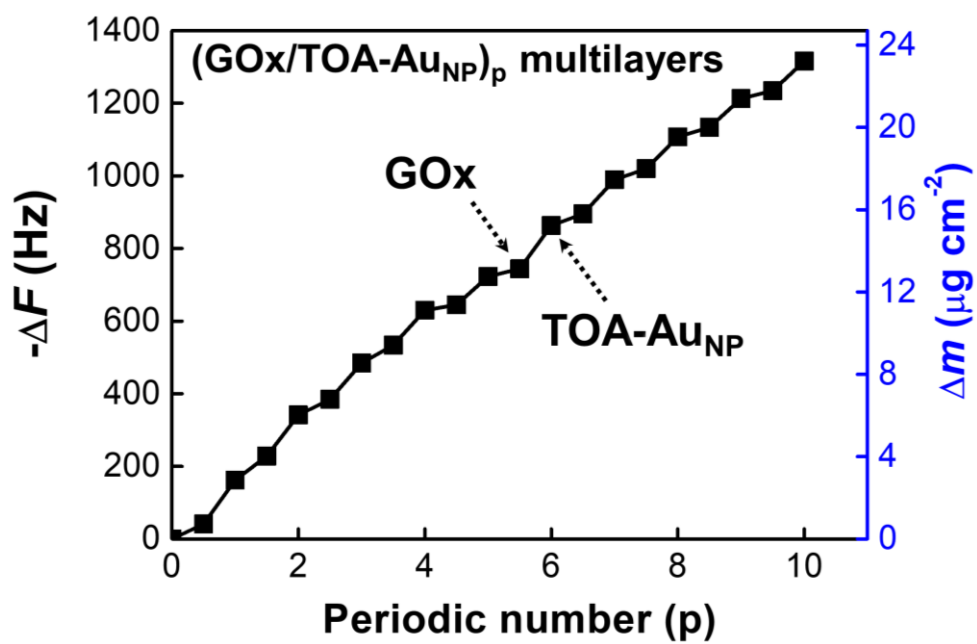
FIG. S13. QCM analysis. QCM measurement of (GOx/TOA-Au$_{NP}$)$_p$ multilayers as a function of periodic number (p).

FIG. S14. Surface morphology and thickness analysis. Planar FE-SEM images of (a) $(GOx/TOA-Au_{NP})_3$, (b) $(GOx/DETA/C-Au_{NP}/DETA)_4$, and (c) $(GOx/DETA)_3$ multilayers onto Si wafers. In this case, 6 nm-sized $TOA-Au_{NP}$ and 23 nm-sized $C-Au_{NP}$ were used for amphiphilic and electrostatic LbL assemblies, respectively. (d) Total film thicknesses of $(GOx/TOA-Au_{NP})_p$ multilayers as a function of periodic layer number (p). The insets show the cross-sectional FE-SEM images of $(GOx/TOA-Au_{NP})_6$ and $(GOx/TOA-Au_{NP})_{15}$.
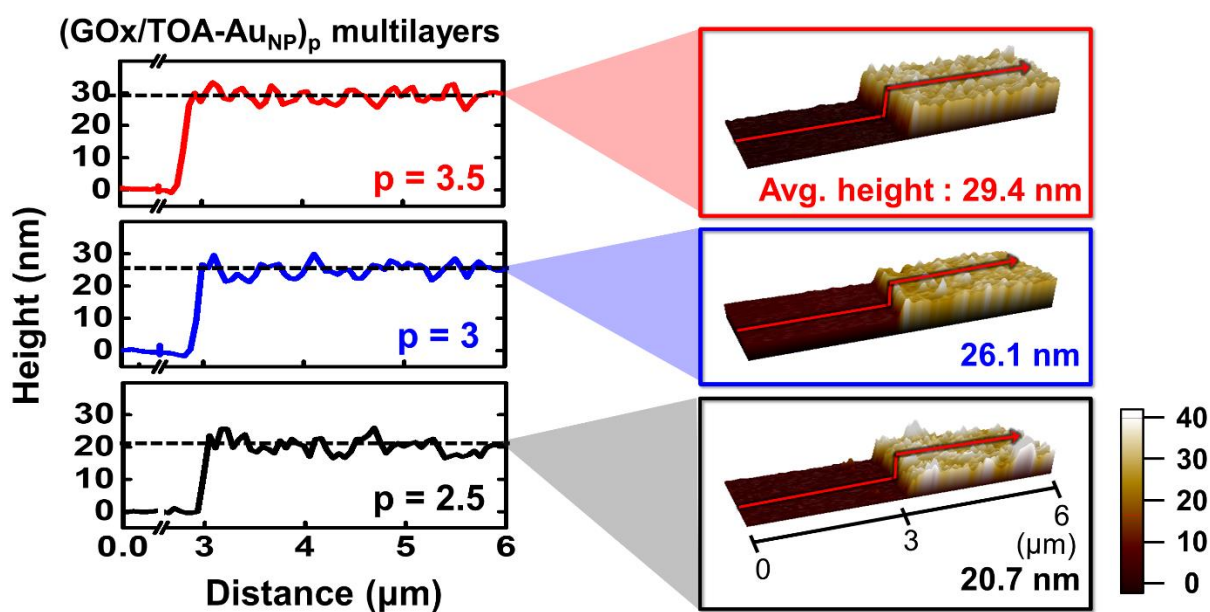
FIG. S15. AFM images. The average height for GOx and TOA-Au$_{NPs}$ layers measured at different p values. As a result, the average layer thicknesses of TOA-Au$_{NP}$ and GOx were measured to be approximately 5.4 nm and 3.3 nm, respectively. The root-mean-square (RMS) roughnesses of (GOx/TOA-Au$_{NP}$)$_{2.5}$, (GOx/TOA-Au$_{NP}$)$_3$, and (GOx/TOA-Au$_{NP}$)$_{3.5}$ multilayers were measured to be approximately 3.3, 7.8, and 7.3 nm, respectively.

(a)

Amide A — Native GOx — Amide I — Amide II

Intensity (a.u.) vs Wavenumber (cm^{-1})

Wavenumber (cm^{-1})	Assignments
3305	Amide A
2920	CH asymmetric stretching in CH$_2$
2856	CH symmetric stretching in CH$_3$
1740	C=O stretching
1640	C=O stretching Amide I
1539	N−H bending Amide II
1378	CH bending CH$_3$
1213	Amide III
1110	C−O stretching

(b)

GOx dipped in toluene

Intensity (a.u.) vs Wavenumber (cm^{-1})

Amide I — Amide II

(c)

C-H stretch (2928, 2856) — TOA-Au$_{NP}$ — C-H scissor (1466)

Intensity (a.u.) vs Wavenumber (cm^{-1})

(d)

(GOx/TOA-Au$_{NP}$)$_3$

Intensity (a.u.) vs Wavenumber (cm^{-1})

(e)

Heat treatment

Intensity (a.u.) vs Wavenumber (cm^{-1})

(f)

EtOH treatment

Intensity (a.u.) vs Wavenumber (cm^{-1})

FIG. S16. FTIR spectra of LbL-assembled GOx. (a) Characteristic FTIR spectra of native GOx on the flat electrode (i.e., Au-coated Si wafer). In this case, the native GOx layer was prepared by drop casting method.[S3,S4] The right panel indicates a list of peak positions and the attributions of native GOx sample and tentative assignment in the FTIR spectrum.[S4] (b) FTIR spectra of GOx measured after immersing the GOx-coated electrode in toluene for 20 min. In this case, the amide I (at 1640 cm^{-1}) and amide II (at 1539 cm^{-1}) bands were still observed. FTIR spectra of (c) TOA-Au$_{NP}$ and (d) (GOx/TOA-Au$_{NP}$)$_3$ multilayers deposited onto the electrode. FTIR spectra of (e) heat- and (f) ethanol-treated GOx samples. For preparing the heat- and ethanol-treated GOx samples, they were dipped in the boiling water of 100 °C and ethanol solution for 1 h, respectively.

In the case of native GOx-coated electrode, two obvious FTIR absorption bands (*i.e.*, the amide I band at 1650 cm^{-1} and II band at 1539 cm^{-1}) originating from amide groups were observed from the native GOx (**Fig. S16(a)**).[S3–S5] Generally, the presence of these amide I and amide II bands evidently implies that the secondary structure and bioactivity of GOx molecules is still preserved after GOx immobilization. Based on this reference data, we also examined the FTIR absorption bands of the GOx-coated electrode dipped in toluene. In this case, their amide bands almost coincided with those of the above-mentioned native GOx-coated electrode (**Fig. S16(b)**). Considering that the toluene solvent was used for the deposition of TOA-Au$_{NPs}$ onto the immobilized GOx layer, these results indicated that toluene solvent had no effect on the bioactivity and conformational change of immobilized GOx layer.

To further confirm these phenomena, we additionally investigated the amide bands of the (GOx/TOA-Au$_{NP}$)$_3$ multilayer-coated electrode. Although the absorption bands of TOA-Au$_{NPs}$ were partially overlapped with those of native GOx layer at 1466 (C-H stretching) and 1378 cm^{-1} (C-H scissor and bending) (**Fig. S16(c)**), TOA ligands were replaced by GOx during their LbL deposition as already mentioned (see **Figs. S3** and **S11**). In addition to this ligand exchange reaction, the typical amide I and II bands of the (GOx/TOA-Au$_{NP}$)$_3$ multilayers could be clearly observed, which was also very similar to those of native GOx layer (**Fig. S16(d)**). These results strongly support the fact that the immobilized GOx layers within the (GOx/TOA-Au$_{NP}$)$_3$ multilayer is in active conformation.

On the other hand, in the case of the thermally (treated by boiling water of 100 °C for 1 h) and chemically (treated by ethanol solution for 1 h) denaturized GOx samples, their FTIR spectra did not exhibit the amide I and amide II absorption bands due to the dissociation of FAD (**Fig. S16(e,f)**). These FTIR results clearly showed that thermally- or chemically-treated GOx samples were denaturized.
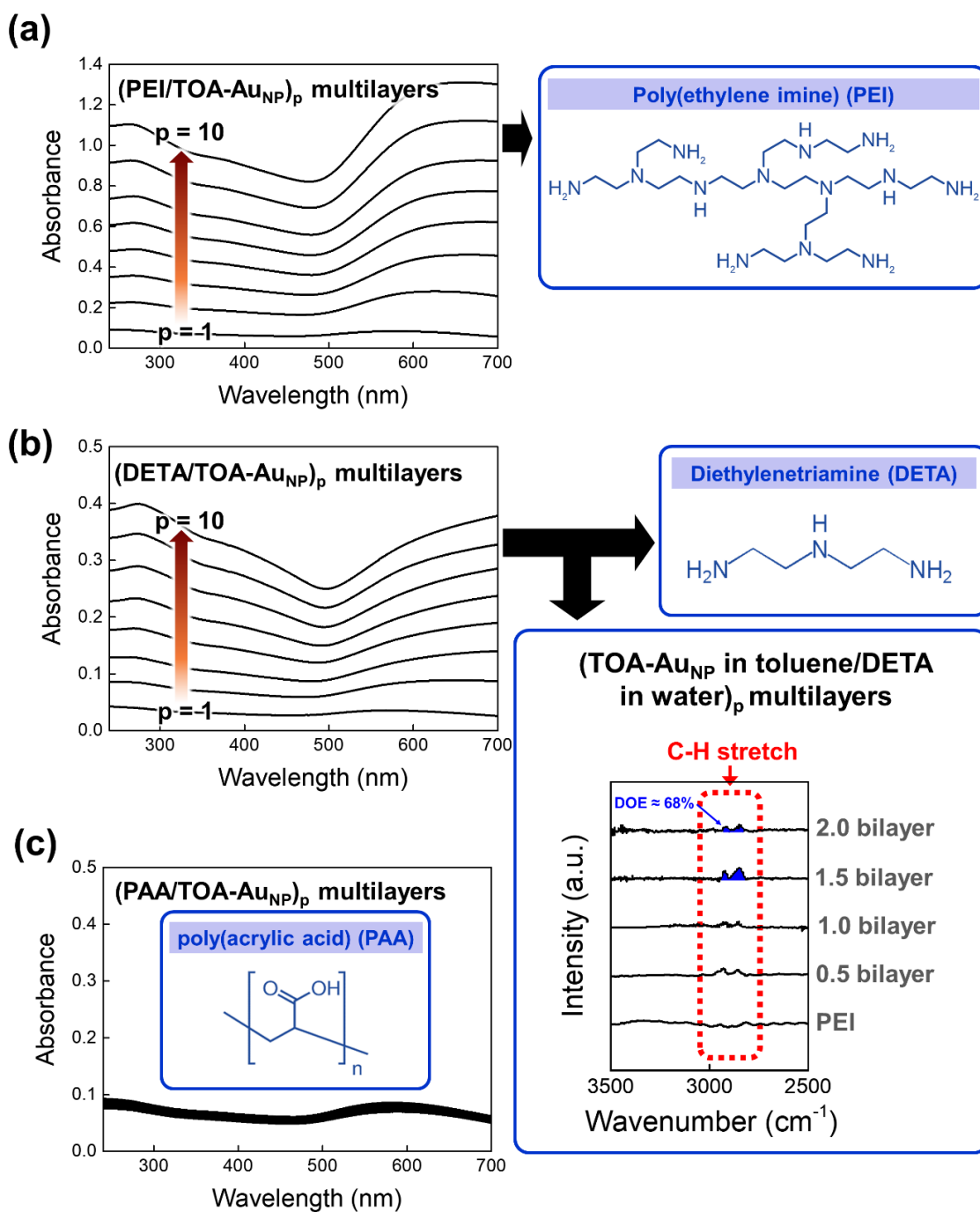
FIG. S17. Optical analysis of multilayers. UV-vis absorbance spectra of (a) (PEI in pH 7.4 water/TOA-Au$_{NP}$ in toluene)$_p$ multilayers, (b) (DETA in pH 7.4 water/TOA-Au$_{NP}$ in toluene)$_p$ multilayers, and (c) (PAA in pH 7.4 water/TOA-Au$_{NP}$ in toluene)$_p$ multilayers measured with increasing the periodic number (p) from 1 to 10. The M$_w$ of PEI and PAA used in our study were 25,000 g mol^{-1} and 1,800 g mol^{-1}, respectively. Additionally, the solution concentrations of PEI, DETA, and PAA were fixed at 2 mg mL^{-1}.
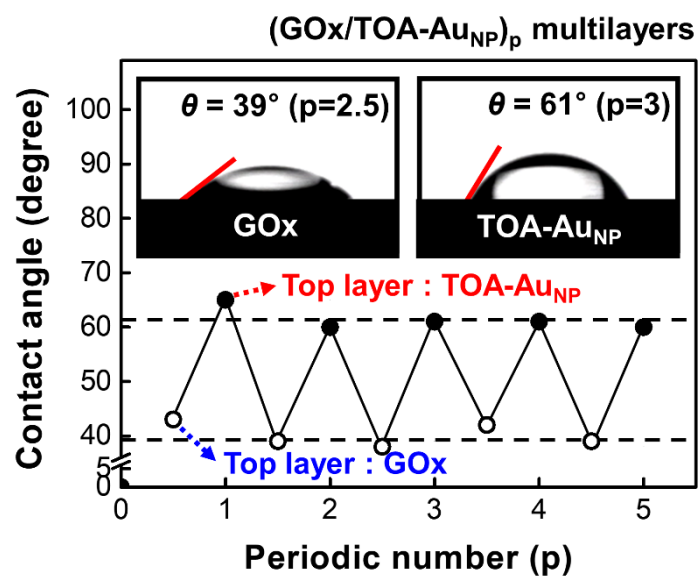
FIG. S18. Deposition mechanism analysis of (GOx/TOA-Au$_{NP}$)$_p$ multilayers. Water contact angles on an Au-sputtered Si wafer with periodic numbers.
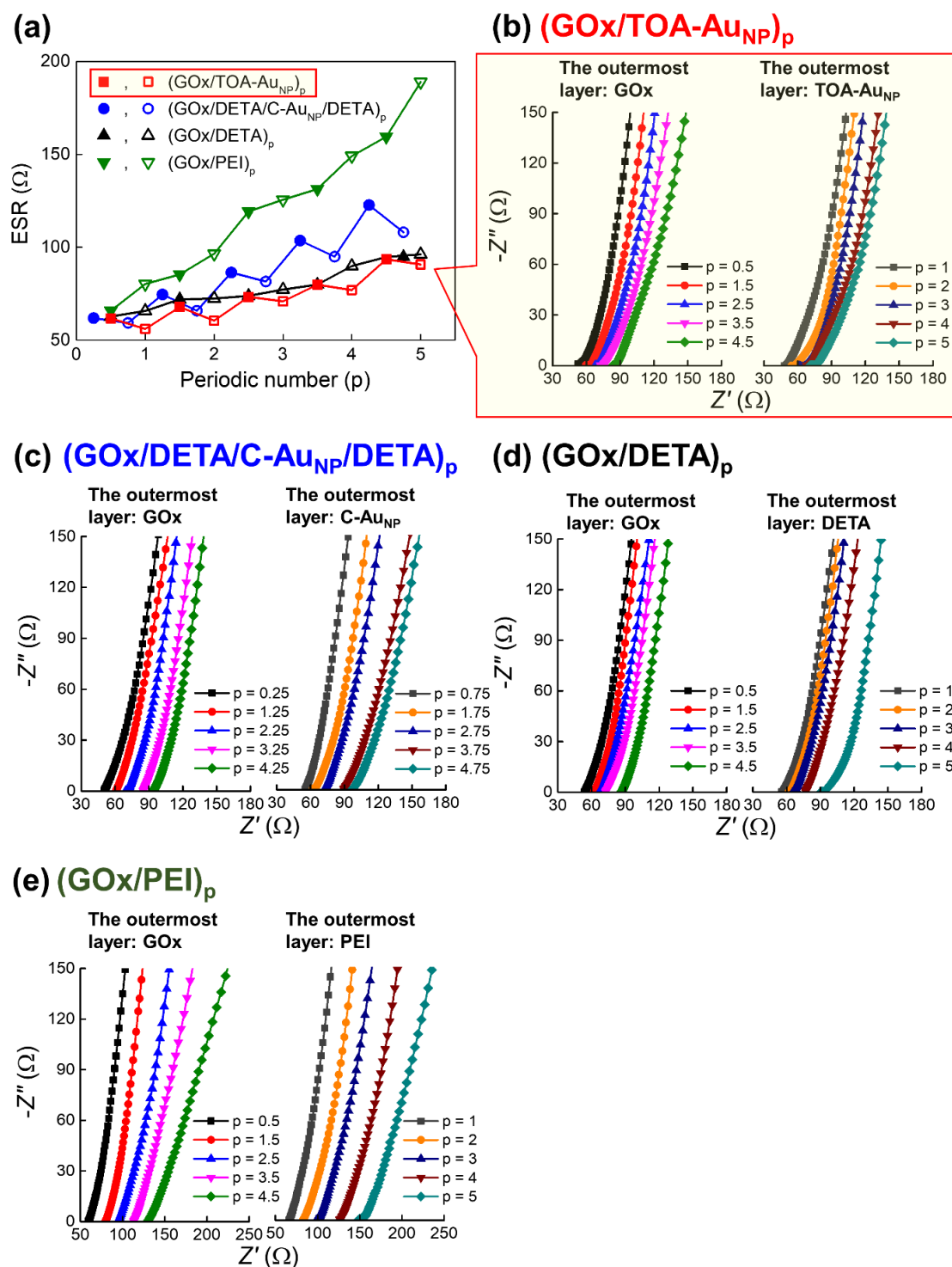
**FIG. S19.** Electrochemical analysis. (a) Change in the ESR values of the $(GOx/TOA\text{-}Au_{NP})_p$, $(GOx/DETA/C\text{-}Au_{NP}/DETA)_p$, $(GOx/DETA)_p$, and $(GOx/PEI)_p$ multilayers with increasing p from 0 to 5. In this case, all the solid symbols indicate the outermost GOx layer. On the other hand, the open symbols indicate the $TOA\text{-}Au_{NP}$, $C\text{-}Au_{NP}$, DETA, and PEI layer as the outermost layer. Nyquist plots of (b) $(GOx/TOA\text{-}Au_{NP})_p$, (c) $(GOx/DETA/C\text{-}Au_{NP}/DETA)_p$, (d) $(GOx/DETA)_p$, and (E) $(GOx/PEI)_p$ multilayers.
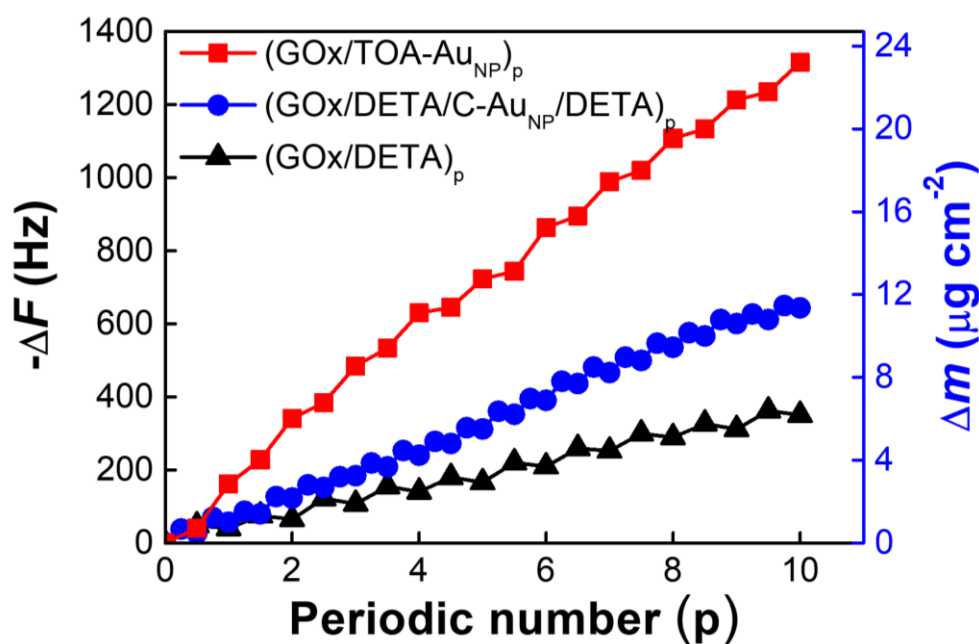
FIG. S20. QCM analysis. Frequency (-ΔF) and mass changes (Δm) of (GOx/TOA-Au$_{NP}$)$_p$, (GOx/DETA/C-Au$_{NP}$/DETA)$_p$, and (GOx/DETA)$_p$ multilayers according to the periodic number (p). In this case, the adsorbed amount of GOx/TOA-Au$_{NP}$ per periodic number was much higher than those of GOx/DETA/C-Au$_{NP}$/DETA and GOx/DETA. Particularly, we highlight that the high loading amount of TOA-Au$_{NPs}$ shown in our amphiphilic assembly cannot be easily realized by the traditional electrostatic LbL assembly with strong electrostatic repulsion between the same charged NPs in water.
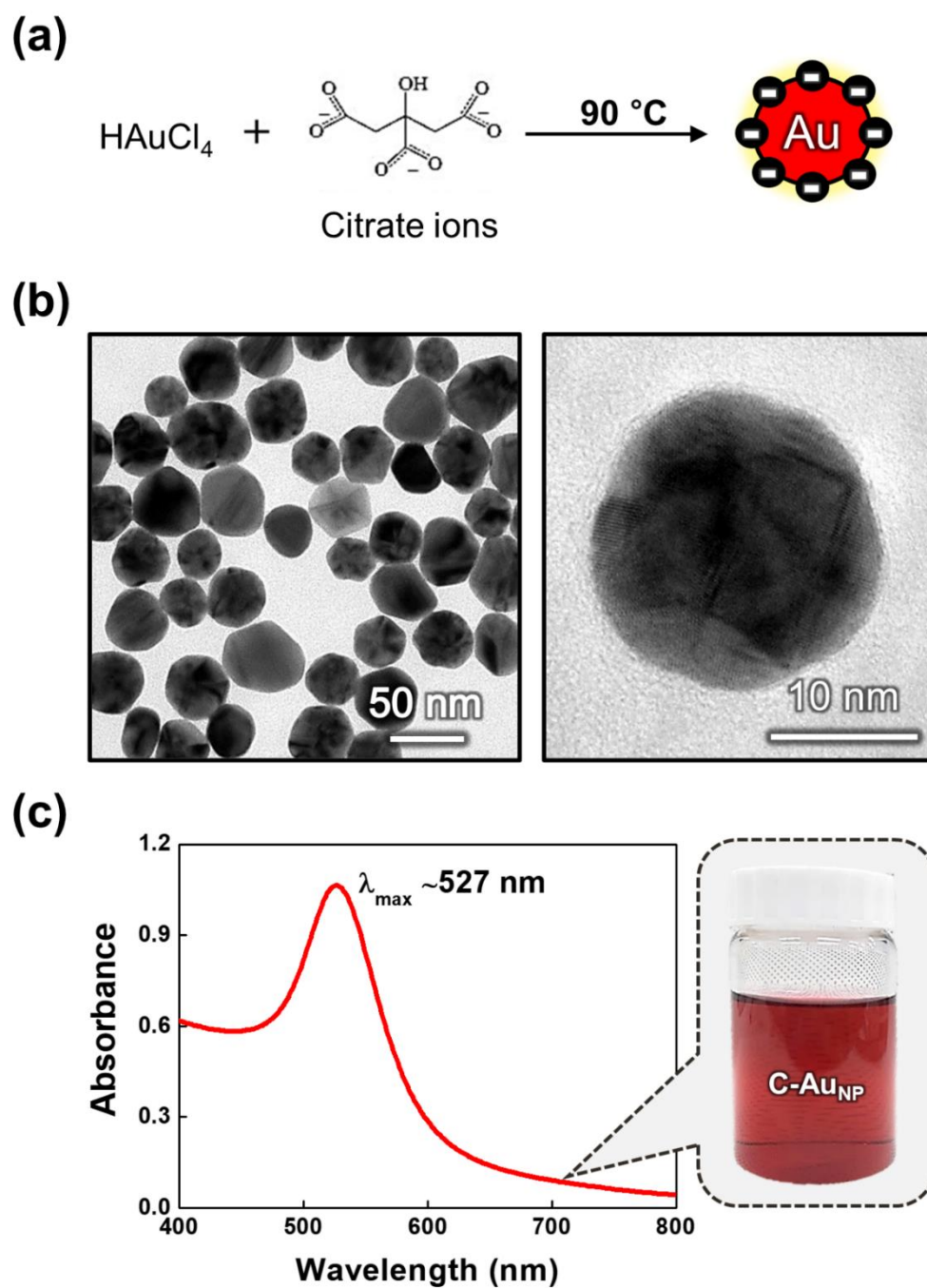
FIG. S21. Citrate ion-stabilized Au_{NP}. (a) Synthesis of anionic citrate ion-stabilized Au_{NP} (C-Au_{NPs}) in water. (b) HR-TEM image of C-Au_{NPs} with a diameter of 23 ± 5 nm. (c) UV-vis spectrum and optical image of C-Au_{NPs} in water.
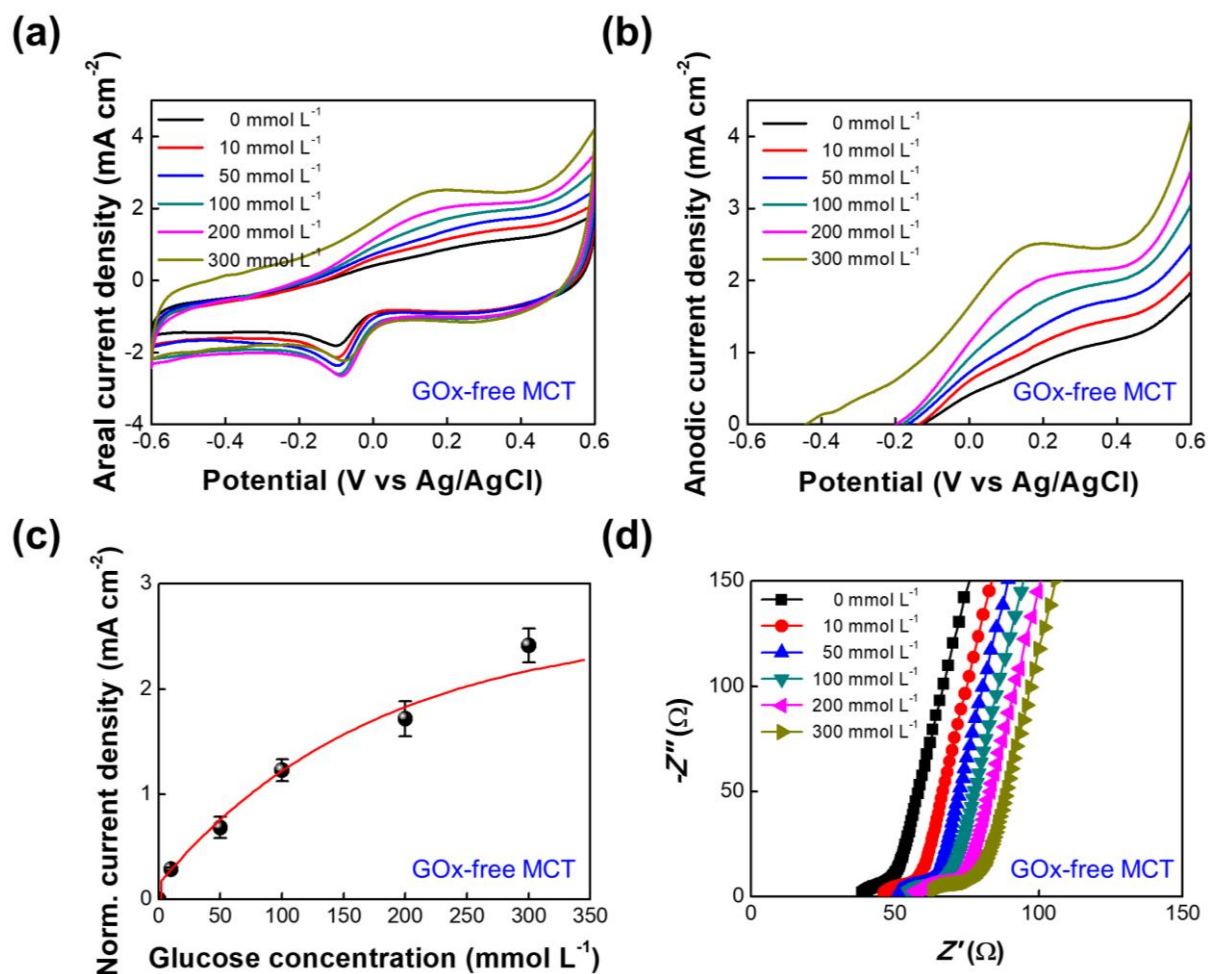
FIG. S22. Electrooxidation effect of bare MCT without GOx. (a) CV curves of bare MCT at a scan rate of 5 mV s^{-1}. (b) Change in anodic current density of GOx-free bare MCT with increasing the glucose concentration from 0 to 300 mmol L^{-1} at a scan rate of 5 mV s^{-1}. (c) The normalized current density (in mA cm^{-2}) showing the electrooxidation activities of GOx-free MCT electrode at different glucose concentrations (from 0 to 300 mmol L^{-1}) at a scan rate of 5 mV s^{-1}. Herein, the normalized current density was obtained by subtracting the current density level in glucose-free PBS at +0.6 V. (d) Nyquist plots of the GOx-free MCT electrode as a function of glucose concentration. With increasing the glucose concentration from 0 to 300 mmol L^{-1}, the ESR values were increased from 37 to 62 Ω. All the electrochemical tests were performed in PBS (pH 7.4) under ambient conditions at 36.5 °C.
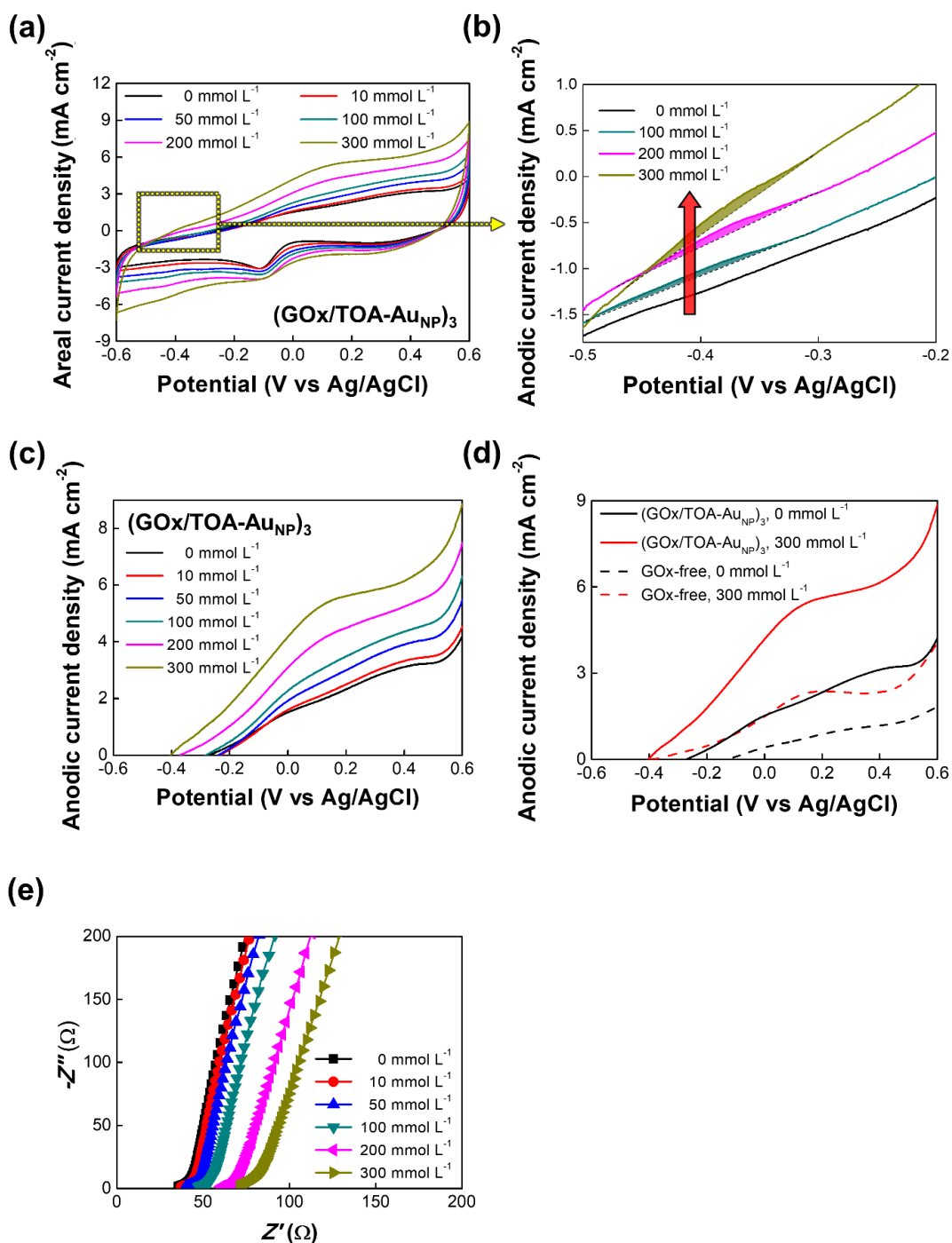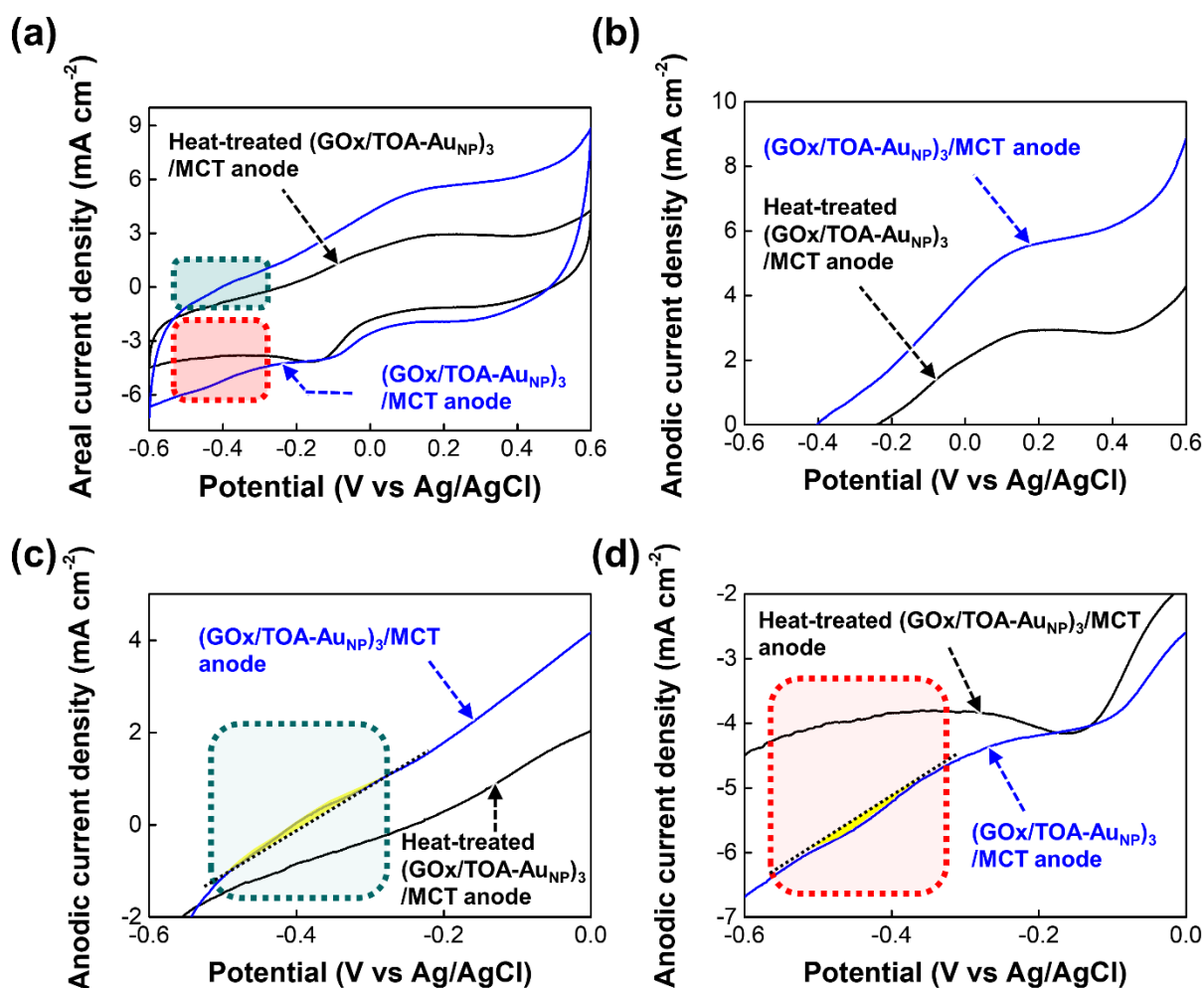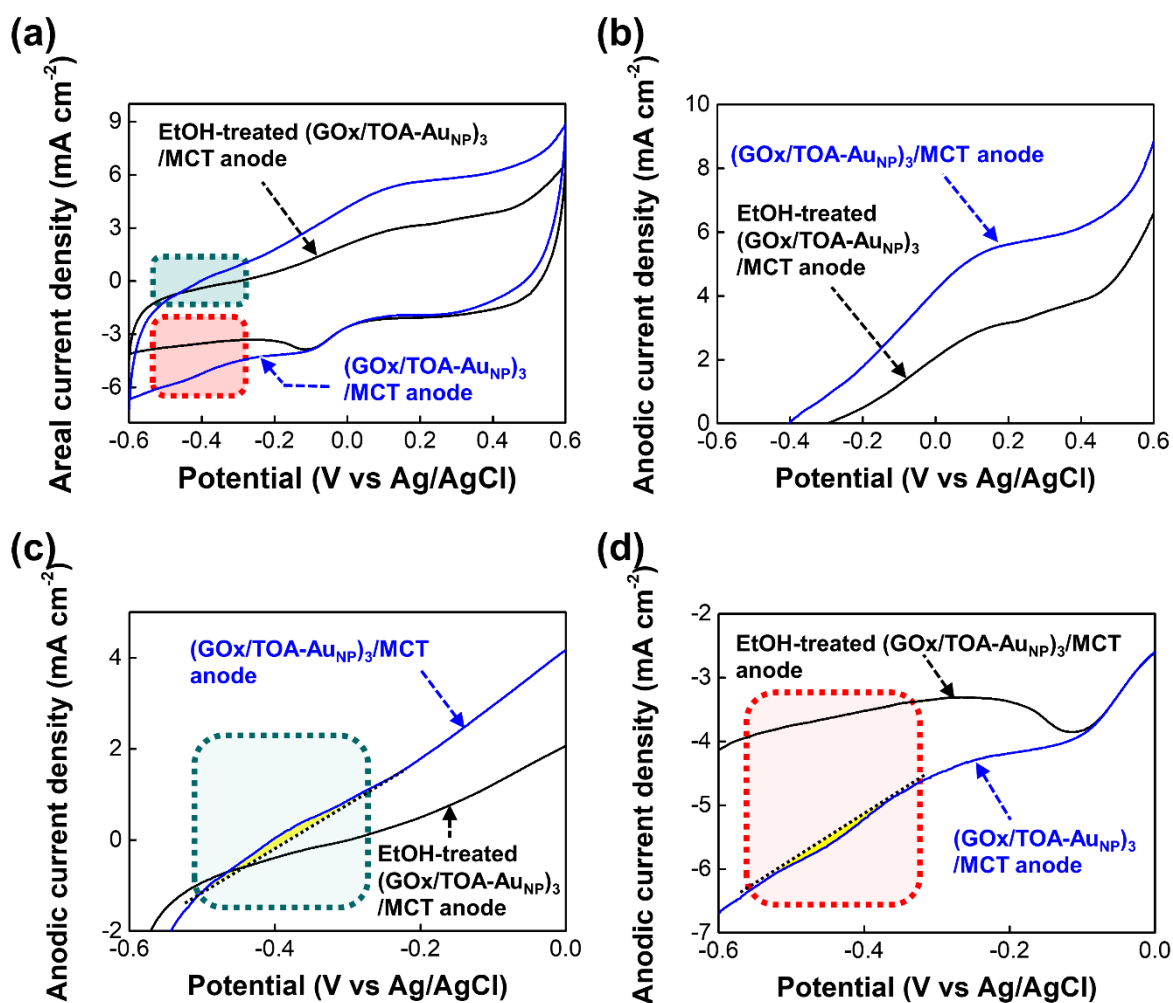
FIG. S23. Electrochemical performance of (GOx/TOA-Au$_{NP}$)$_3$/MCT anode. (a) CVs of the (GOx/TOA-Au$_{NP}$)$_3$/MCT as a function of glucose concentration. (b) Evidence of DET between GOx and MCT substrate obtained from (a). (c) Anodic current density of the plots obtained from (a). (d) Anodic current densities of (GOx/TOA-Au$_{NP}$)$_3$/MCT and bare MCT measured at the glucose concentrations of 0 and 300 mmol L^{-1}. All electrochemical measurements were performed at a scan rate of 5 in PBS under ambient conditions at 36.5 °C. (e) Nyquist plots of GOx-assembled anodes with increasing the glucose concentration from 0 to 300 mmol L^{-1} glucose in PBS (pH 7.4).
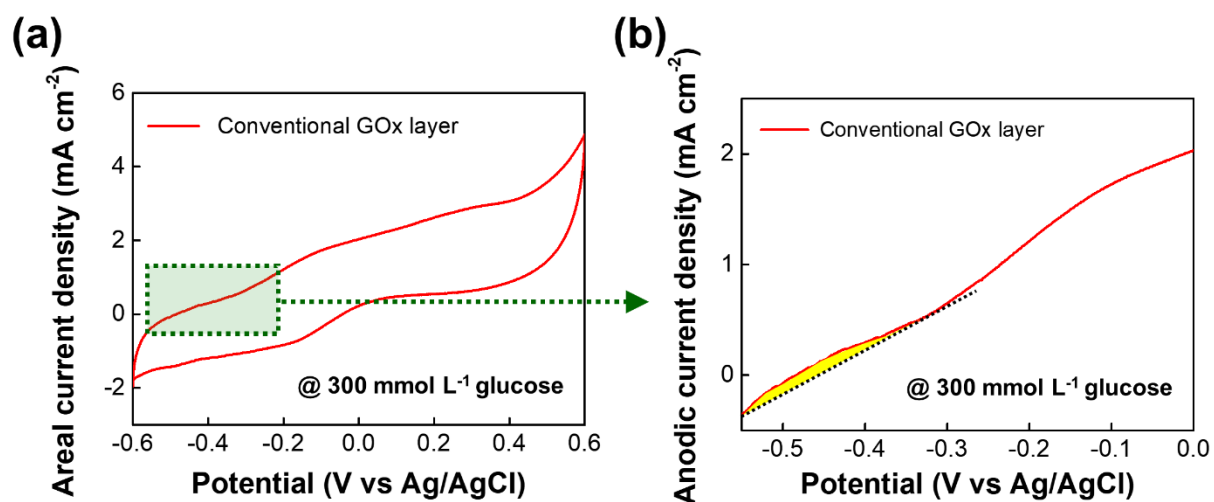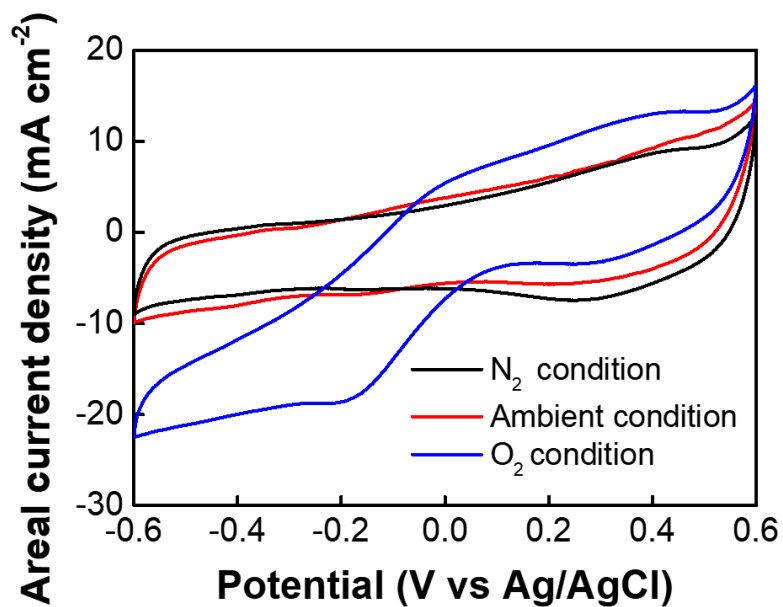
FIG. S24. Electrochemical performance of conventional GOx electrode. (a) CV. (b) Evidence of DET between GOx and TOA-Au$_{NP}$ obtained from the oxidation curve of (a).
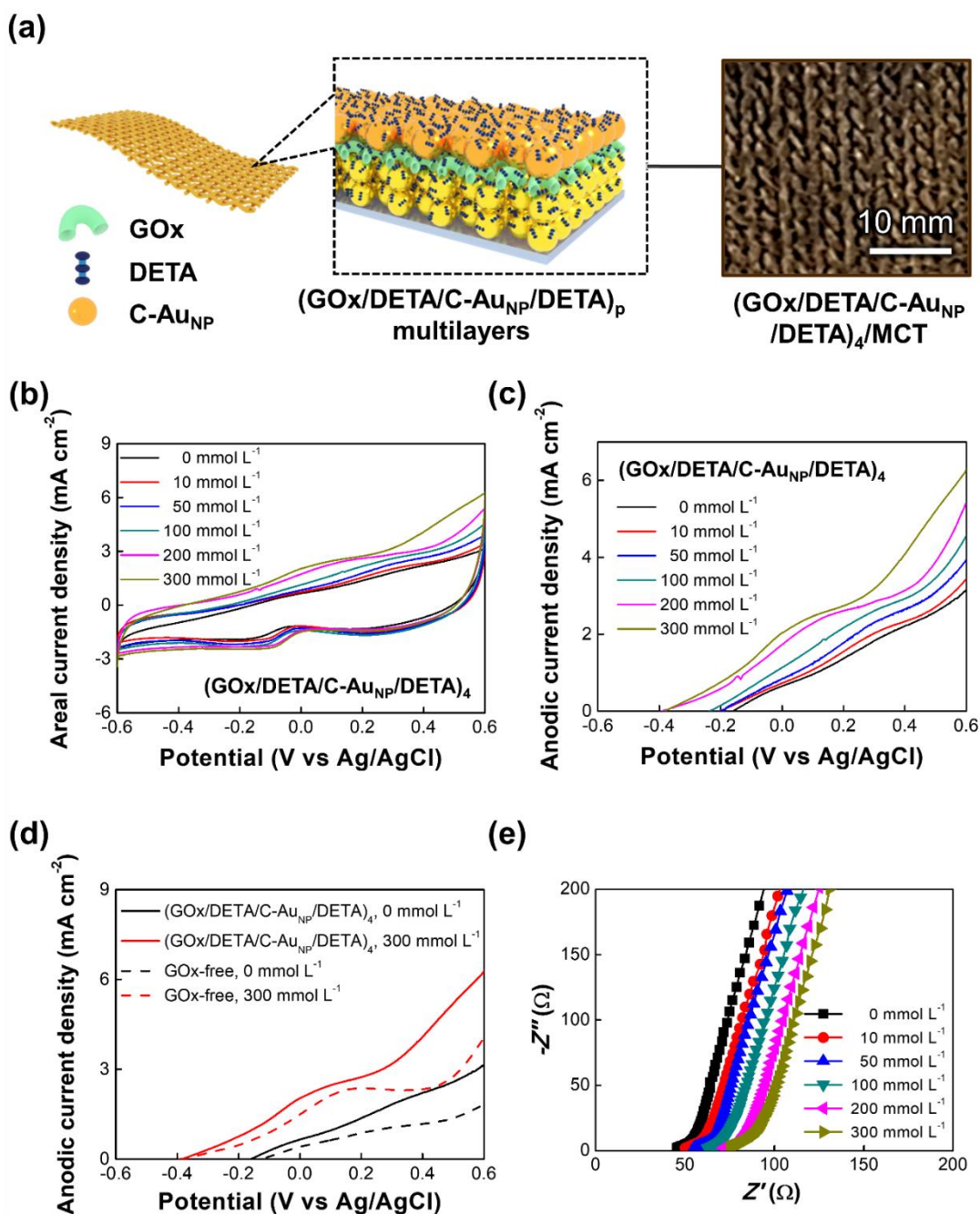
Fig. S25. Electrochemical performance of denatured enzyme control based on the heat-treated (GOx/TOA-Au$_{NP}$)$_3$/MCT anode. (a) CVs and (b) Anodic current density curves of (GOx/TOA-Au$_{NP}$)$_3$/MCT anode under ambient conditions. (c) Evidence of DET between GOx and TOA-Au$_{NP}$ obtained from the oxidation curve shown in (a). (d) Evidence of DET between GOx and TOA-Au$_{NP}$ obtained from the reduction curve shown in (a). In the case of the heat-treated (GOx/TOA-Au$_{NP}$)$_3$/MCT anode, two specific oxidation and reduction GOx peaks, which are observed at −0.41 and −0.45 V, respectively, were clearly disappeared. For preparing the heat-treated anode, the (GOx/TOA-Au$_{NP}$)$_3$/MCT electrode was dipped in the boiling water of 100 °C for 1 h.

27

Fig. S26. Electrochemical performance of denatured enzyme control based on an ethanol-treated (GOx/TOA-Au$_{NP}$)$_3$/MCT anode. (a) CVs and (b) Anodic current density curves of (GOx/TOA-Au$_{NP}$)$_3$/MCT anode under ambient conditions. (c) Evidence of DET between GOx and TOA-Au$_{NP}$ obtained from the oxidation curve shown in (a). (d) Evidence of DET between GOx and TOA-Au$_{NP}$ obtained from reduction curve shown in (a). In the case of ethanol-treated (GOx/TOA-Au$_{NP}$)$_3$/MCT anode, two specific oxidation and reduction GOx peaks, which are observed at −0.41 and −0.45 V, respectively, were clearly disappeared. For preparing the ethanol-treated anode, it was dipped in the ethanol solution for 1 h.
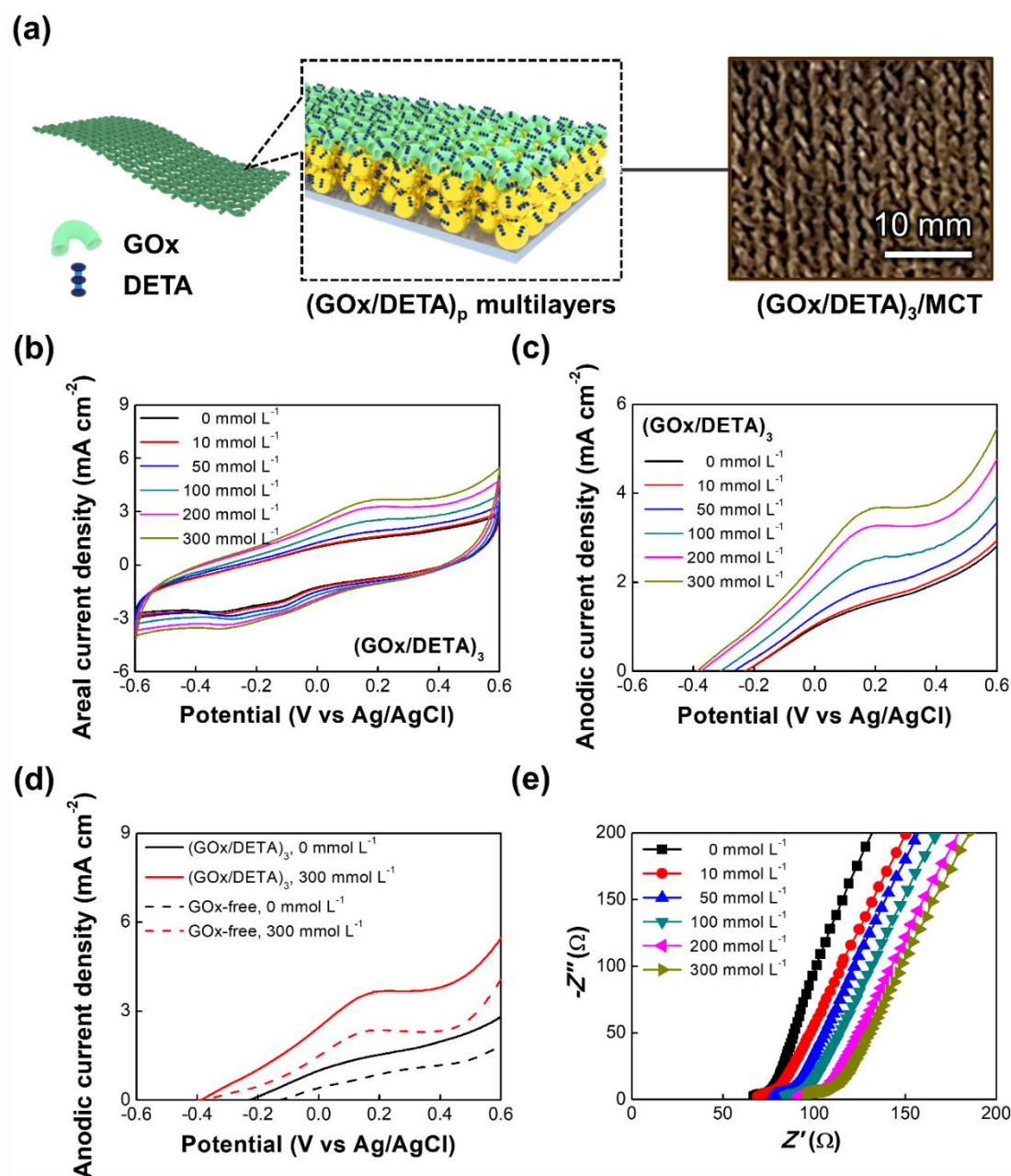
FIG. S27. Electrochemical performance of (GOx/TOA-Au$_{NP}$)$_3$/MCT anodes. CVs of (GOx/TOA-Au$_{NP}$)$_3$/MCT anode under N$_2$-saturated, ambient, and O$_2$-saturated conditions.

FIG. S28. Electrochemical performance of (GOx/DETA/C-Au$_{NP}$/DETA)$_4$/MCT anode. (a) Scheme of (GOx/DETA/C-Au$_{NP}$/DETA)$_p$/MCT (left side) and optical image (right side). (b) CVs of (GOx/DETA/C-Au$_{NP}$/DETA)$_4$/MCT as a function of the glucose concentration. In this case, the detailed layer structure of (GOx/DETA/C-Au$_{NP}$/DETA)$_p$ is (anionic GOx/cationic DETA/anionic C-Au$_{NP}$/cationic DETA)$_p$ based on electrostatic interaction between anionic and cationic components. (c) Anodic current density curves of (GOx/DETA/C-Au$_{NP}$/DETA)$_4$/MCT as a function of glucose concentration. The areal current densities of (GOx/DETA/C-Au$_{NP}$/DETA)$_4$/MCT were measured with increasing the glucose concentration from 0 to 300

mmol L^{-1}. (d) Anodic current density curves of the (GOx/DETA/C-Au$_{NP}$/DETA)$_4$/MCT and the bare MCT electrode without GOx measured at the two different glucose concentrations of 0 and 300 mmol L^{-1}. (e) Nyquist plots of (GOx/DETA/C-Au$_{NP}$/DETA)$_4$/MCT with increasing the glucose concentration from 0 to 300 mmol L^{-1}. All the electrochemical measurements shown in (b-e) were performed at a scan rate of 5 mV s^{-1} in PBS buffer solution under ambient conditions.

FIG. S29. Electrochemical performance of (GOx/DETA)₃/MCT anode. (a) Scheme of (GOx/DETA)ₚ/MCT (left side) and optical image (right side). (b) CVs of (GOx/DETA)₃/MCT as a function of the glucose concentration. (c) Anodic current density curves of (GOx/DETA)₃/MCT as a function of the glucose concentration. The areal current densities of (GOx/DETA)₃/MCT were measured with increasing the glucose concentration from 0 to 300 mmol L^{-1}. (d) Anodic current density curves of the (GOx/DETA)₃/MCT and the bare MCT electrode without GOx measured at the two different glucose concentrations of 0 and 300 mmol L^{-1}. (e) Nyquist plots of (GOx/DETA)₃/MCT with increasing the glucose concentration from 0 to 300 mmol L^{-1}. All the electrochemical measurements shown in (b-e) were performed at a scan rate of 5 mV s^{-1} in PBS buffer solution under ambient conditions.
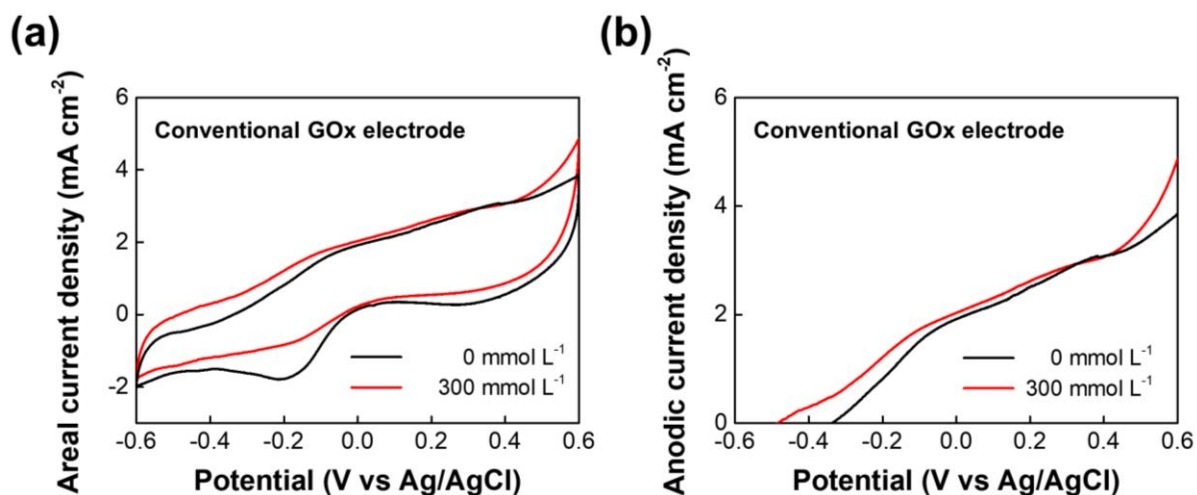
FIG. S30. Electrochemical performance of conventional GOx/MCT electrode. (a) CVs and (b) anodic current density curves of conventionally blended GOx/MCT electrodes. The current densities of the anodes were measured in 0 mmol L^{-1} and 300 mmol L^{-1} glucose in PBS. All measurements were performed at a scan rate of 5 mV s^{-1} under ambient conditions. For preparing the conventionally blended GOx/MCT anode, GOx were first blended with cross-linking polymer (i.e., poly(ethylene glycol) diglycidyl ether (PEGDGE 400), 7 wt%). After that, the MCT were immersed in the formed slurry for one day, and then dried in ambient condition.
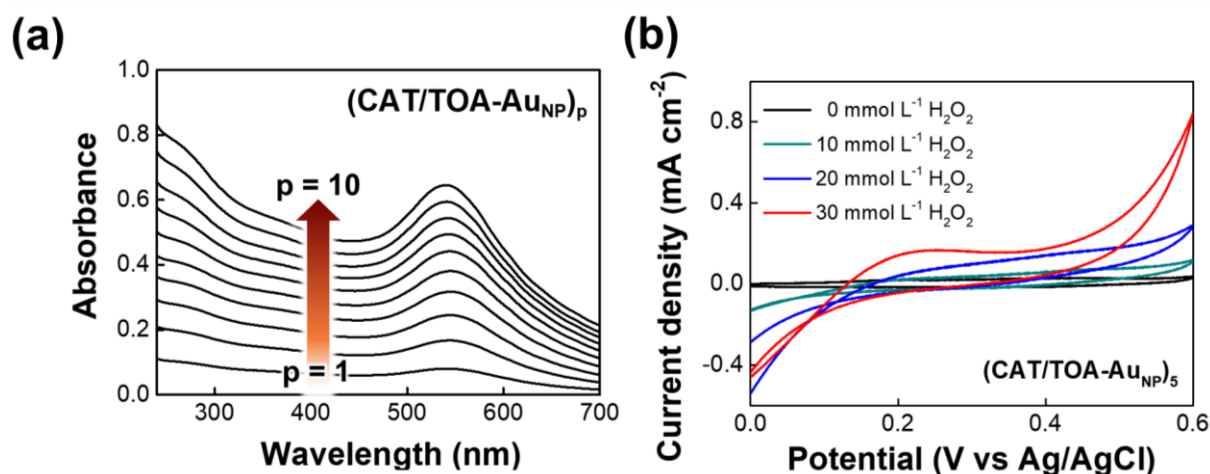
FIG. S31. Catalytic activity of (CAT/TOA-Au$_{NP}$) multilayers. (a) UV-vis absorbance spectra. UV-vis spectra of (CAT/TOA-Au$_{NP}$)$_p$ multilayers. (b) CVs of the (CAT/TOA-Au$_{NP}$)$_5$ multilayers on the Au-coated Si wafer. In this case, 0.5 M NaCl was added to 1 mg mL^{-1} CAT aqueous solution. The PBS buffer solutions with four different concentrations of H$_2$O$_2$ (0, 10, 20, and 30 mmol L^{-1}) were used as electrolyte solutions. These results imply that CAT (in water) can also be well-combined with hydrophobic TOA-Au$_{NPs}$ (in toluene), which can significantly enhance electrocatalytic performance toward H$_2$O$_2$.
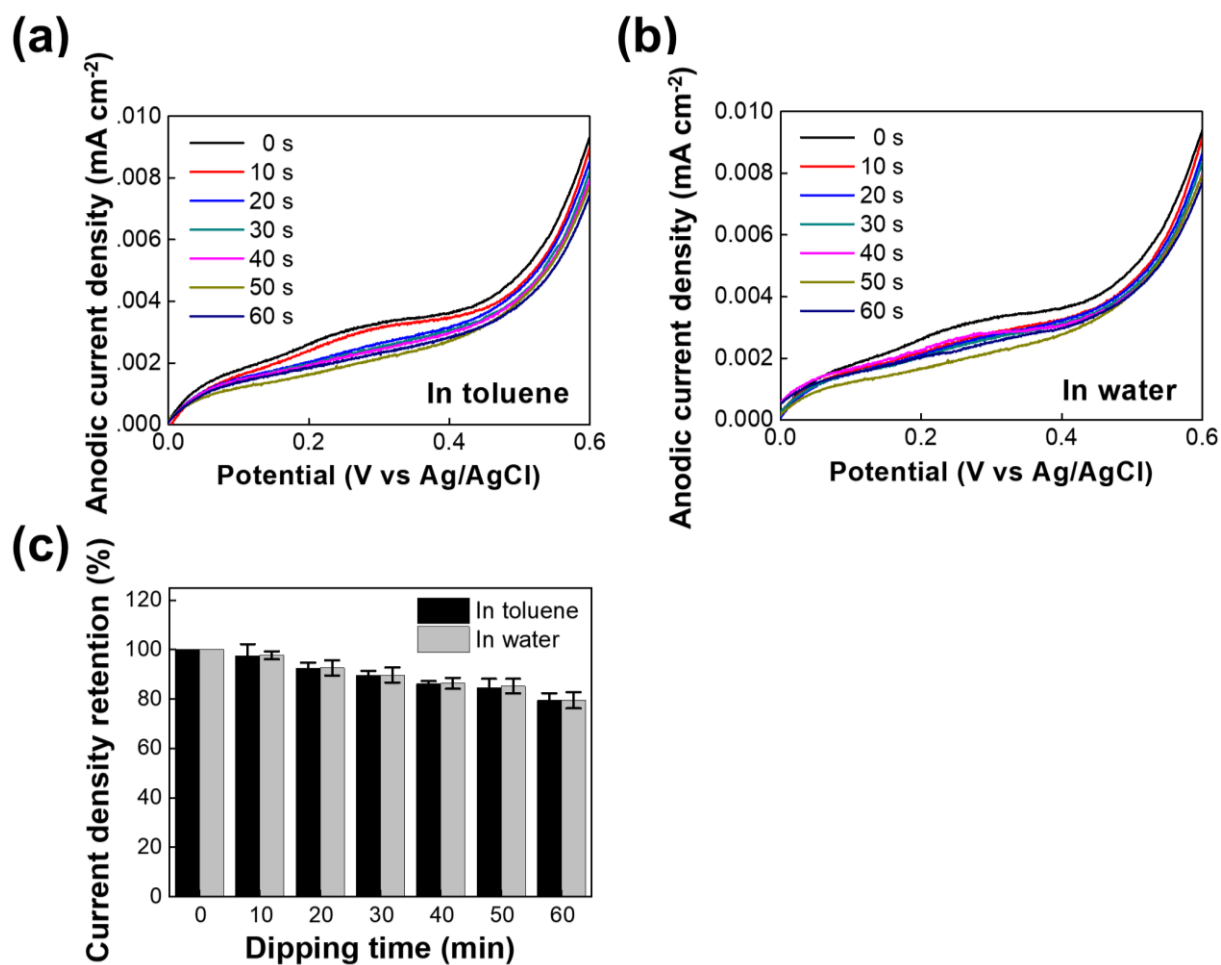
FIG. S32. Current density retention (%) test in toluene and water. Current densities of (GOx/DETA)$_3$ multilayer-coated flat electrodes (i.e., Au-sputtered Si wafer electrodes) measured in aqueous 300 mmol L^{-1} glucose in PBS after the given dipping time in (a) toluene and (b) water. (c) Current density retention (%) of (GOx/DETA)$_3$ multilayer-coated electrodes calculated from the current densities at +0.6 V in (a) and (b). All the measurements related to the current density retention test in water were performed after completely removing residual toluene solvent from anode through air drying.
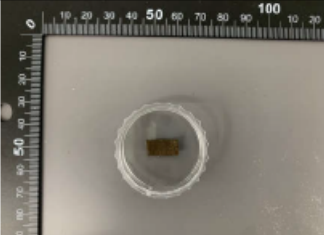
TEST REPORT

Table 1. Sample Information

No.	Sample Name	Koptri ID	Picture of the Sample
1	Metallic Cotton textile containing gold nanoparticles and glucose oxidase, (GOx/TOA-AuNP)5/MCT anode	Koptri-21-07-02068	

Table 2. Test Result

| Koptri ID	Test Item	Unit	Test Method	LOD	Test Result
Koptri-21-07-02068	Toluene	mg/kg	GC-FID	1	N.D.

Note 1) mg/kg = ppm
2) Koptri-VI20-SW0.05-EA-TH5
3) GC-FID; Gas Chromatography – Flame Ionization Detection
4) N.D.; Not Detected

End of Test Report.

**FIG. S33.** Residual toluene within $(GOx/TOA-Au_{NP})_5/MCT$. The amount of residual toluene within the $(GOx/TOA-Au_{NP})_5/MCT$ anode measured from GC-FID (Gas Chromatography – Flame Ionization Detection) at the Korea Polymer Testing & Research Institute (Koptri, Seoul, Korea). The residual toluene within the $(GOx/TOA-Au_{NP})_5/MCT$ anode prepared from our amphiphilic assembly was not detected.
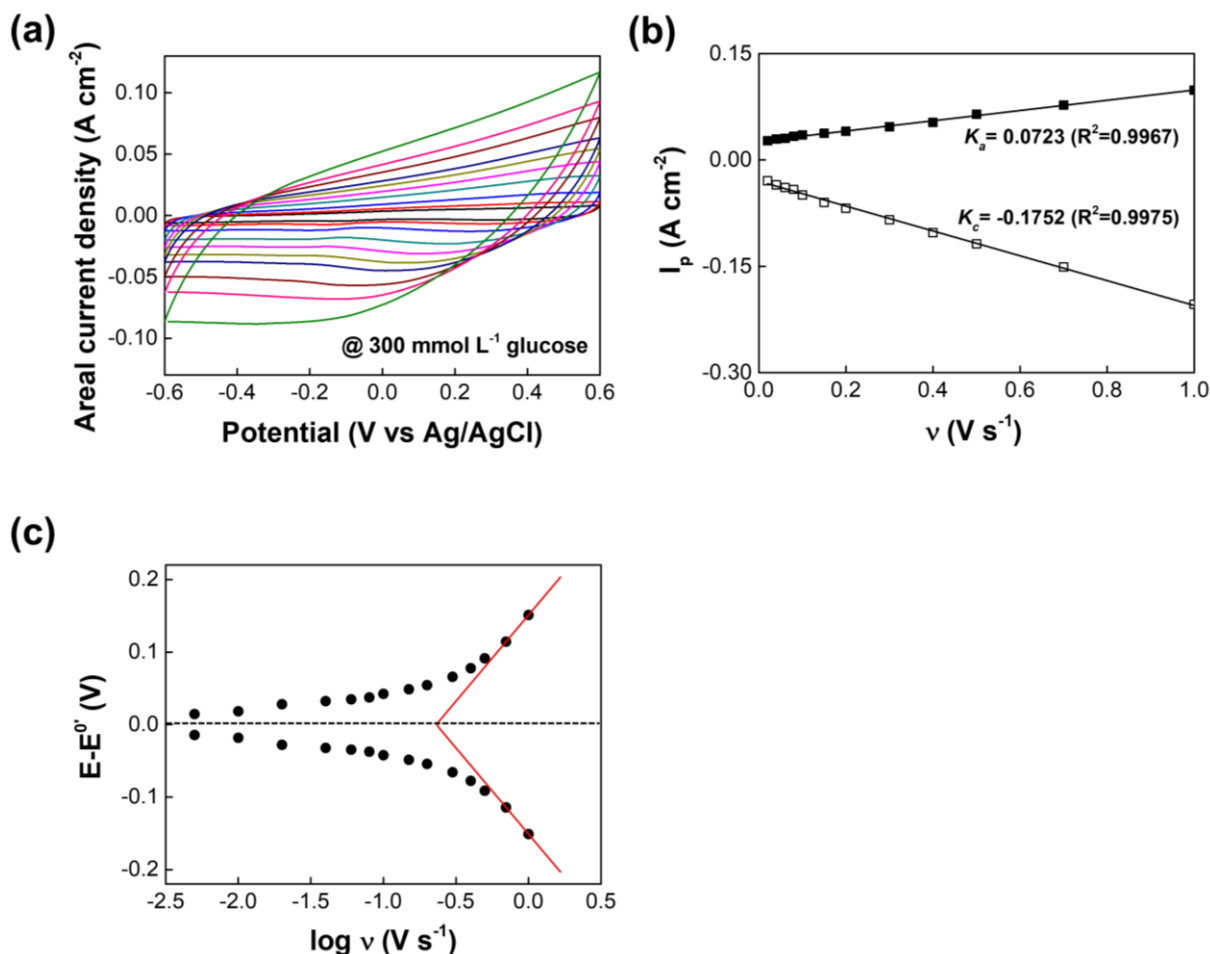
FIG. S34. Electrochemical response of the $(GOx/TOA\text{-}Au_{NP})_3/MCT$ anode. (a) Scan rate-dependent CVs of $(GOx/TOA\text{-}Au_{NP})_3/MCT$ anode in the 300 mmol L^{-1} glucose-containing PBS buffer solution. In this case, the scan rates (from inner to outer) of 0.005, 0.01, 0.02, 0.04, 0.06, 0.08, 0.1, 0.15, 0.2, and 0.3 V s^{-1} were used for electrochemical response measurements. (b) Change in the peak current of the $(GOx/TOA\text{-}Au_{NP})_3/MCT$ anode with increasing the scan rate (v) from 0.02 to 1 V s^{-1}. (c) Change in the potential $(E-E^{0'})$ of $(GOx/TOA\text{-}Au_{NP})_3/MCT$ anode as a function of log (v).

Generally, a large K_s implies an effective reaction that can facilitate the direct electron transfer (DET) of GOx. The K_s value of the anode was calculated from the plot of the separation potential $(\Delta E_p = E \text{ - } E_0)$ vs. log (v) at high scan rates. The $(GOx/TOA\text{-}AuNP)_3/MCT$ anode exhibited a high K_s value of 5.3 ± 0.2 s^{-1}. The DET of $(GOx/TOA\text{-}Au_{NP})_p/MCT$ anode was more favorable than that of previously reported BFC anodes (e.g, 0.3 s^{-1} for a single-walled CNT-modified anode, 1.53 s^{-1} for a multi-walled CNT-modified anode, and 3.96 s^{-1} for a nanostructured porous TiO_2 anode).[S6,S7]

Particularly, considering that the electrochemical response of GOx-immobilized surface is mainly due to the redox reaction of electrochemically active sites (flavin adenine dinucleotide, FAD)[S8] buried within GOx, the small ΔE_p of ~0.10 V in our system indicates a fast heterogeneous electron transfer process that is governed by a surface-controlled reaction rather than a diffusion-controlled reaction. In the case of a surface-controlled system, the ΔE_p is estimated to be less than 0.2 V.[S7] As a result, the small ΔE_p of the (GOx/TOA-Au$_{NP}$)$_3$/MCT anode indicates that fast electron transfer can occur between the redox center of the enzyme and the surface of the MCT with an aid of LbL-assembled Au$_{NP}$ layer.
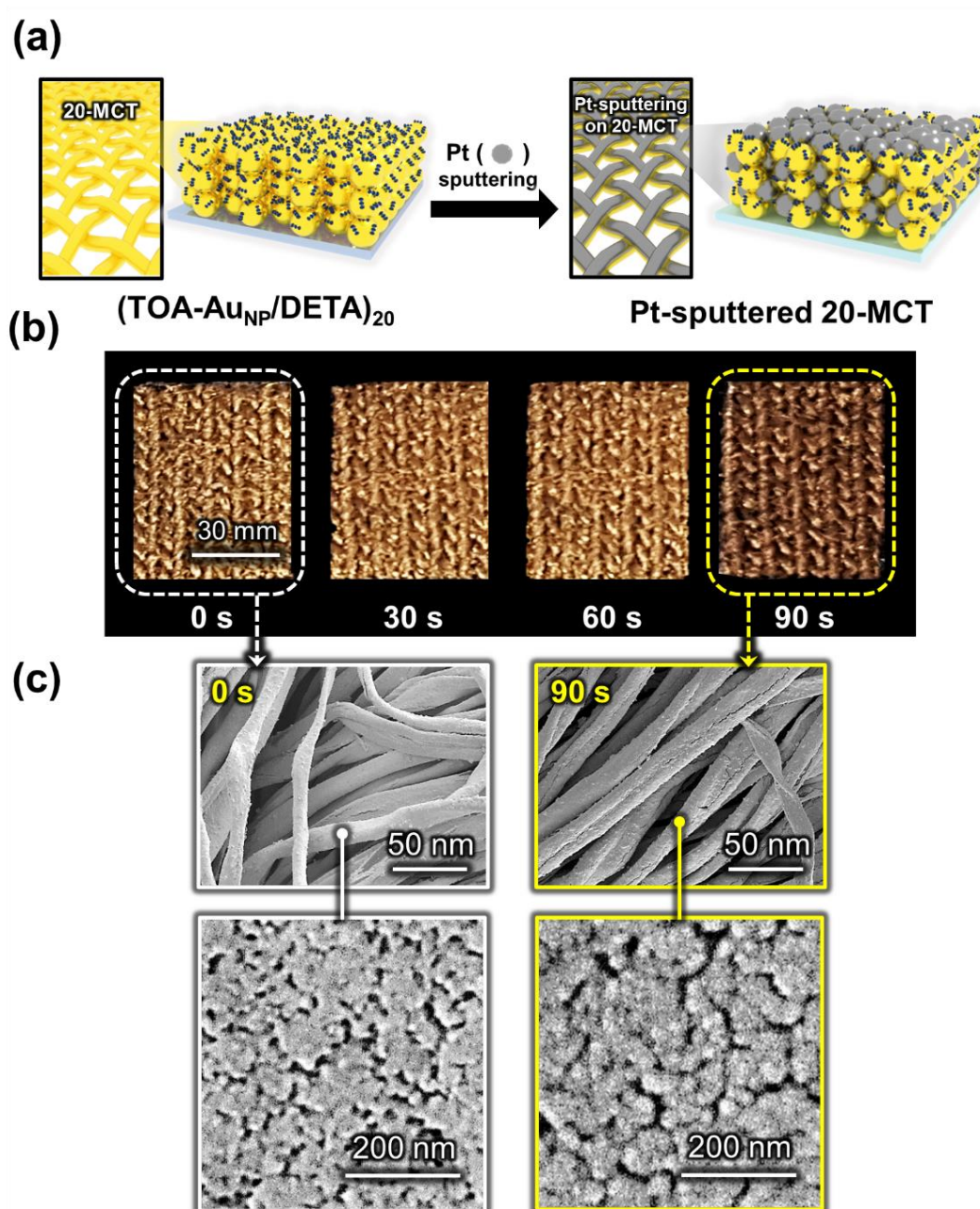
FIG. S35. Catalytic metal-sputtered cathode. (a) Schematic of the preparation of Pt-sputtered MCT (Pt-MCT) cathodes. (b) Optical images of Pt-MCT cathodes prepared by sputtering for different times (0, 30, 60, and 90 s). (c) Planar FE-SEM images of Pt-MCTs sputtered for 0 and 90 s.
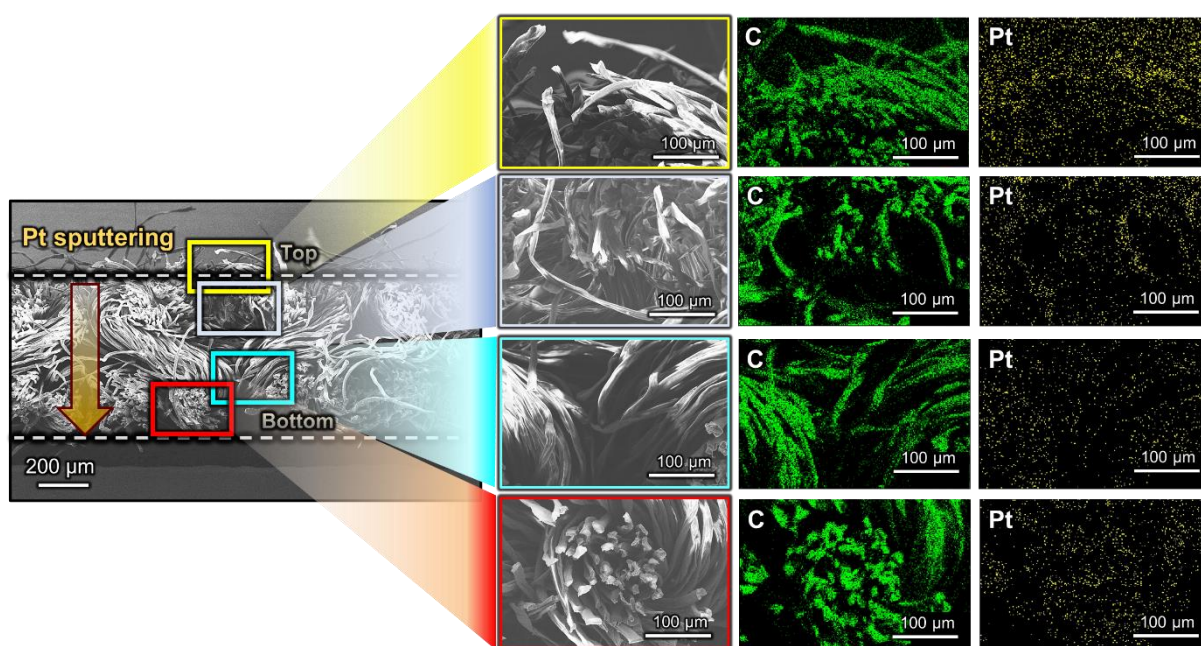
FIG. S36. Pt-sputtered cotton textile. Cross-sectional FE-SEM images and corresponding EDS mapping images of cotton textile after Pt-sputtering for 90 s. Green and yellow dots indicate carbon (C) and platinum (Pt), respectively. For more precisely investigating the depth profile of the sputtered Pt into the textile, a bare cotton textile without TOA-Au$_{NPs}$ was used instead of MCT because Au and Pt cannot be clearly differentiated from EDS mapping due to their similar binding energies. Additionally, Pt was sputtered onto the one side of bare cotton textile. On the other hand, in the case of preparing the cathode, Pt was sputtered onto both sides of MCT.
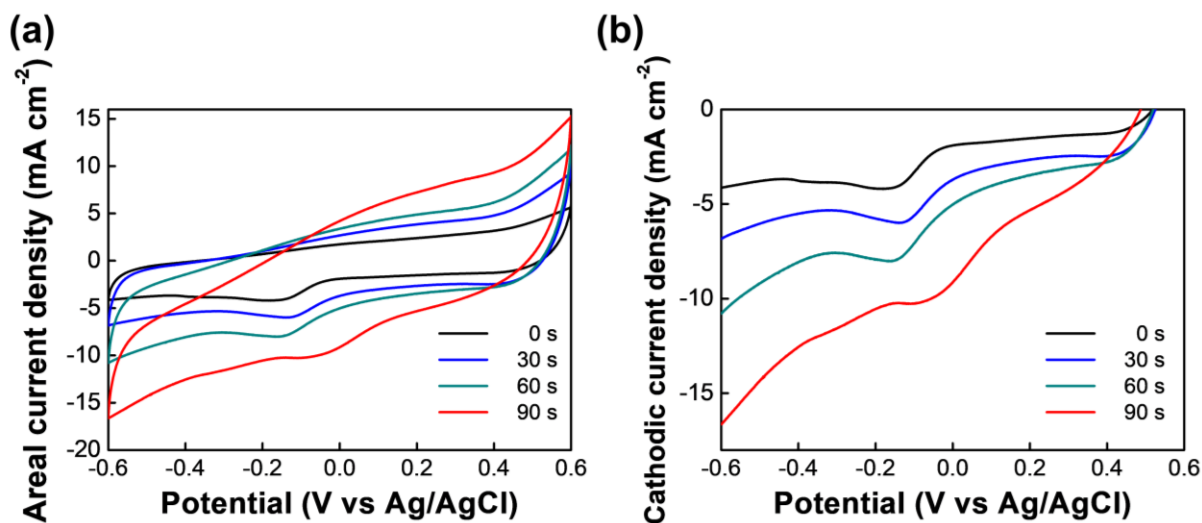
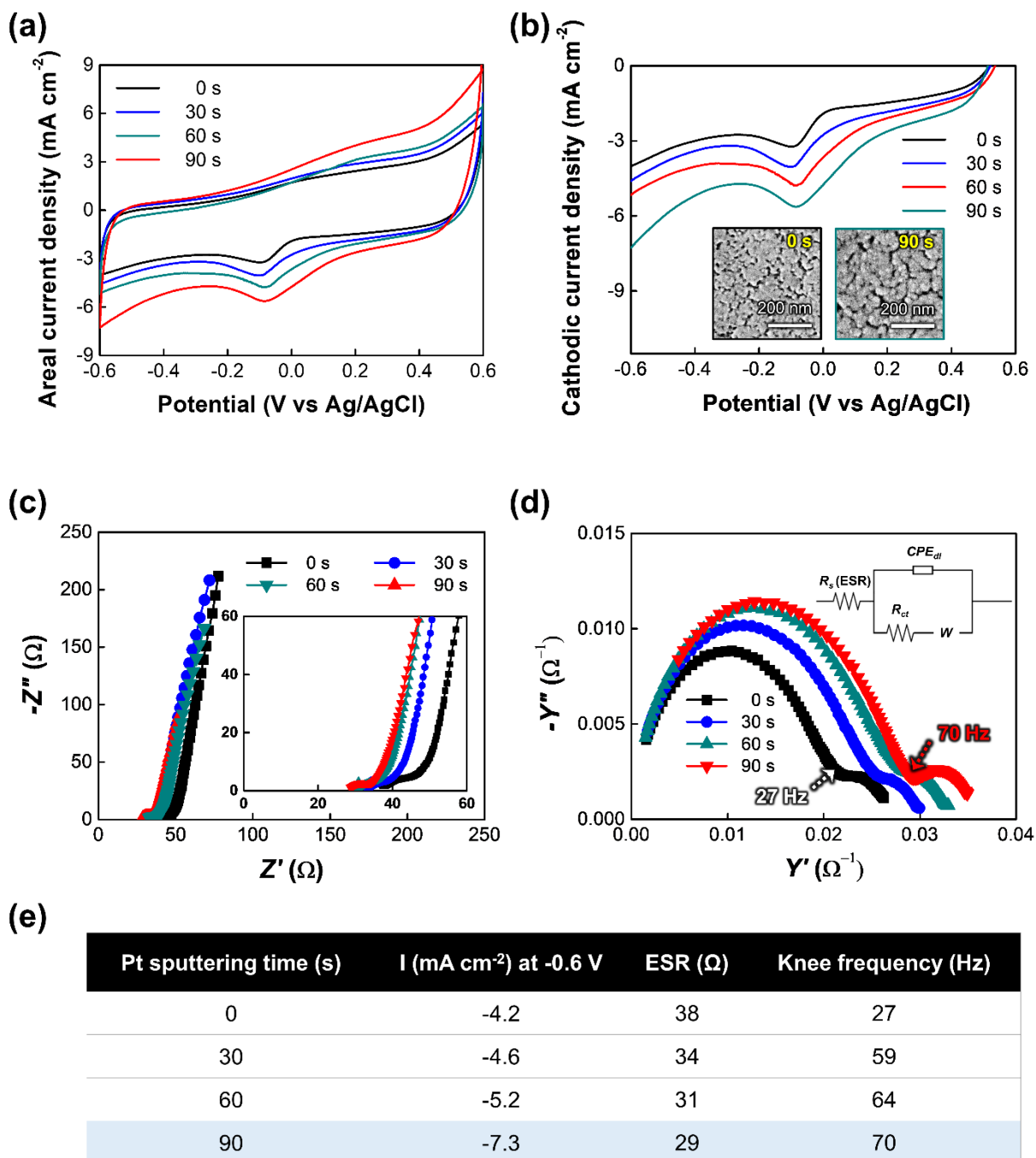**FIG. S37.** Pt-sputtered MCT for cathode. (a) CV curves and (b) cathodic current density curves of the Pt-sputtered MCT (i.e., Pt-MCT) as a function of Pt sputtering time. All the electrochemical measurements were performed at a scan rate of 5 mV s^{-1} in PBS under ambient condition. Additionally, the MCT used for cathode is the 20-MCT (i.e., (TOA-Au$_{NP}$/GOx)$_{20}$-coated cotton textile).
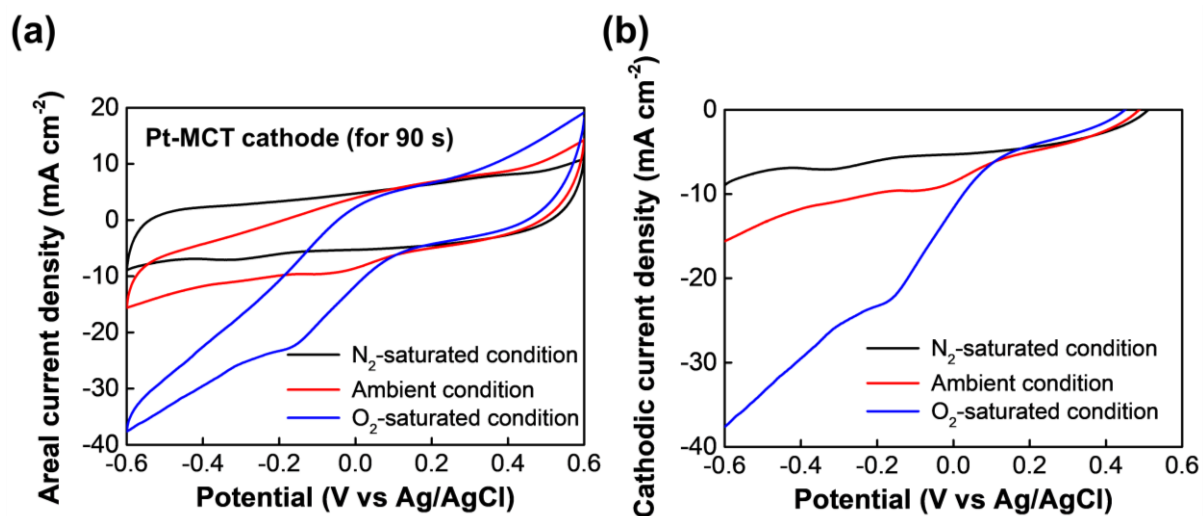
**FIG. S38.** Cathodic performance. (a) CVs and (b) cathodic current density curves of Pt-MCTs under N$_2$-saturated, ambient, and O$_2$-saturated condition.

FIG. S39. One-sided Pt-sputtered MCT cathode. (a) CV curves and (b) cathodic current curves of Pt-MCTs (specifically Pt-20-MCTs) as a function of Pt sputtering time. The insets of (b) show the planar SEM images of MCTs measured from Pt sputtering time of 0 s (Pt-free) and 90 s. (c) Nyquist plots of Pt-MCTs with increasing the Pt sputtering time from 0 to 90 s. Herein, the ESR values measured after the sputtering time of 0, 30, 60, and 90 s were approximately 38, 34, 31, and 29 Ω, respectively. (d) Admittance plots of Pt-MCTs as a function of Pt sputtering time. In this case, labeled frequency values indicate the knee frequency. Here, the Pt-MCT prepared from the sputtering time of 90 s exhibited a relatively high knee frequency

of 70 Hz in comparison with those obtained from other sputtering times (27 Hz for 0 s, 59 Hz for 30 s, 64 Hz for 60 s), which is closely related to the enhancement of charge transport. The inset of (d) shows the representative equivalent circuit from the Nyquist plots. Each impedance component value was obtained from fitting the Randle's equivalent circuit composed of R_s, R_{ct}, constant phase element ($CPEdl$), and W that correspond to the equivalent series resistance (ESR), the charge transfer resistance, the double-layer capacitance, and the Warburg impedance, respectively. (e) Table summarizing the current densities, ESRs, and knee frequencies of Pt-MCTs according to the sputtering time. The cathodic current density level was measured at the potential of −0.6 V (from **FIG. S39(b)**) at a scan rate of 5 mV s^{-1}. All electrochemical measurements were performed in PBS under ambient conditions. Especially, the Pt thickness sputtered for 90 s in our system was measured to be approximately 22.5 nm.
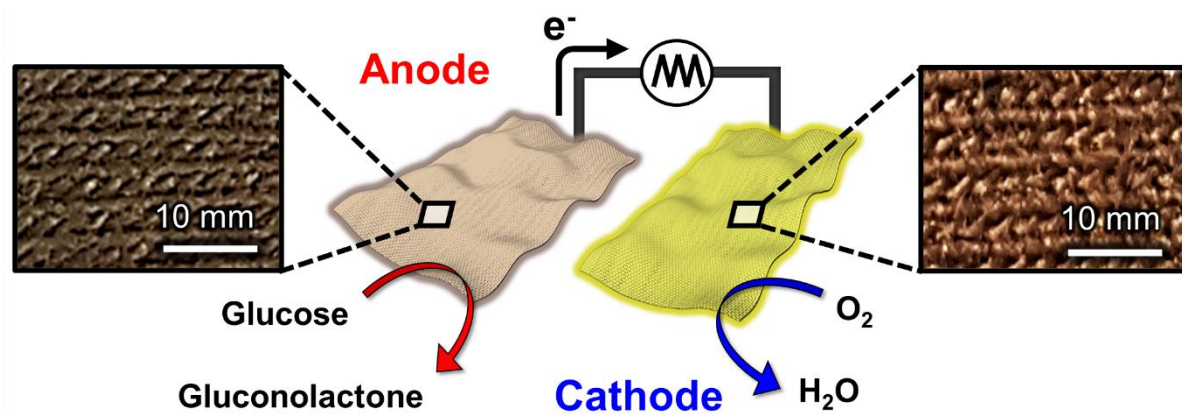
FIG. S40. Schematic diagram of amphiphilic assembly-based biofuel cells (BFCs). The complete BFC composed of (GOx/TOA-Au$_{NP}$)$_3$/MCT anode and Pt-MCT cathode. In this case, the power densities of BFC were determined by measuring the current flowing through external variable resistors (from 1 kΩ – 10 GΩ) to control the cell potential.
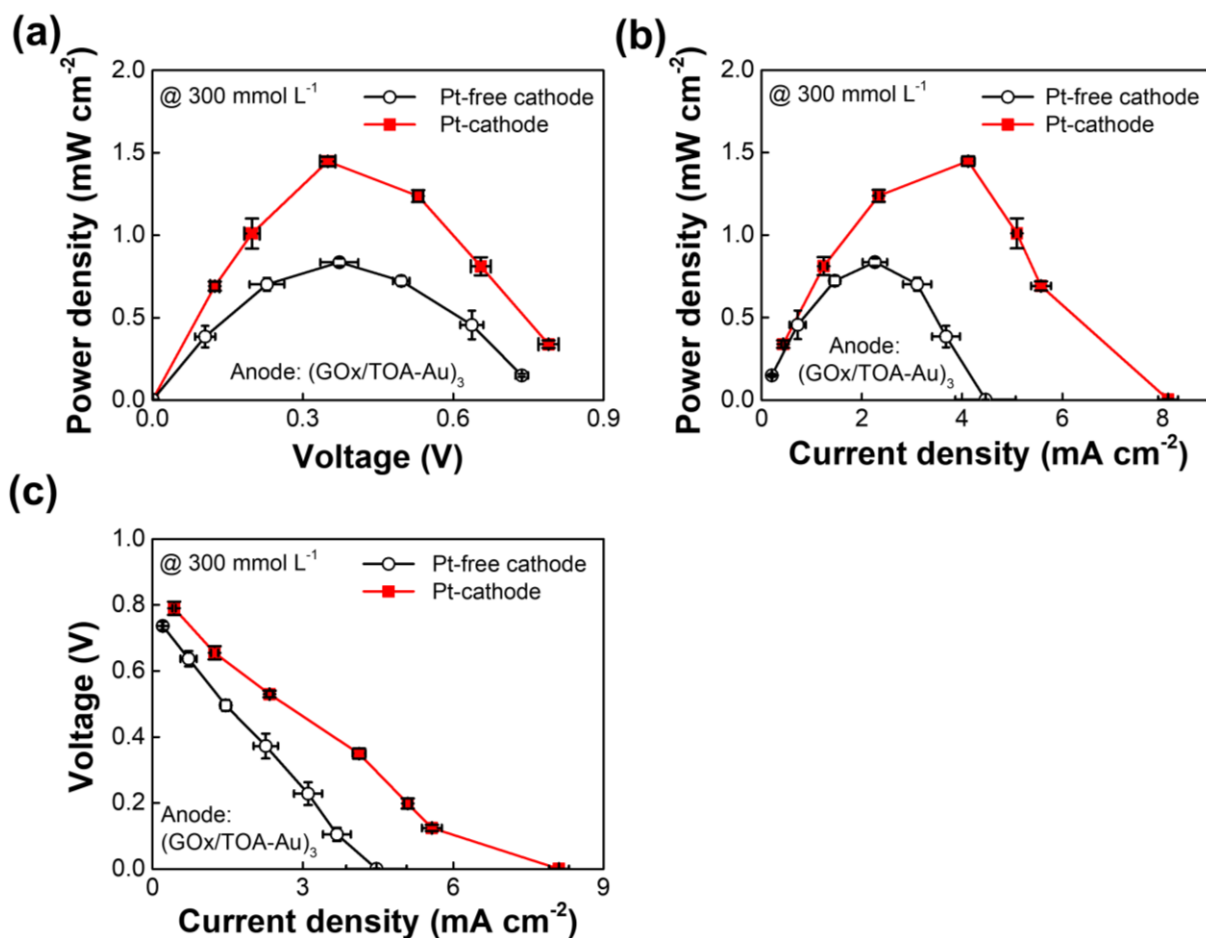
FIG. S41. Effect of Pt-sputtered MCT on power density of BFCs. (a) Power–voltage, (b) power–current, and (c) voltage–current profiles of two different type of the complete BFCs with varying external resistances from 1 kΩ to 10 GΩ. In this case, one BFC was composed of (GOx/TOA-Au$_{NP}$)$_3$/MCT anode// Pt-MCT cathode (red), and the other was composed of (GOx/TOA-Au$_{NP}$)$_3$/MCT anode//Pt-free MCT cathode (black). All measurements were performed in PBS with 300 mmol L^{-1} glucose at 36.5 °C.
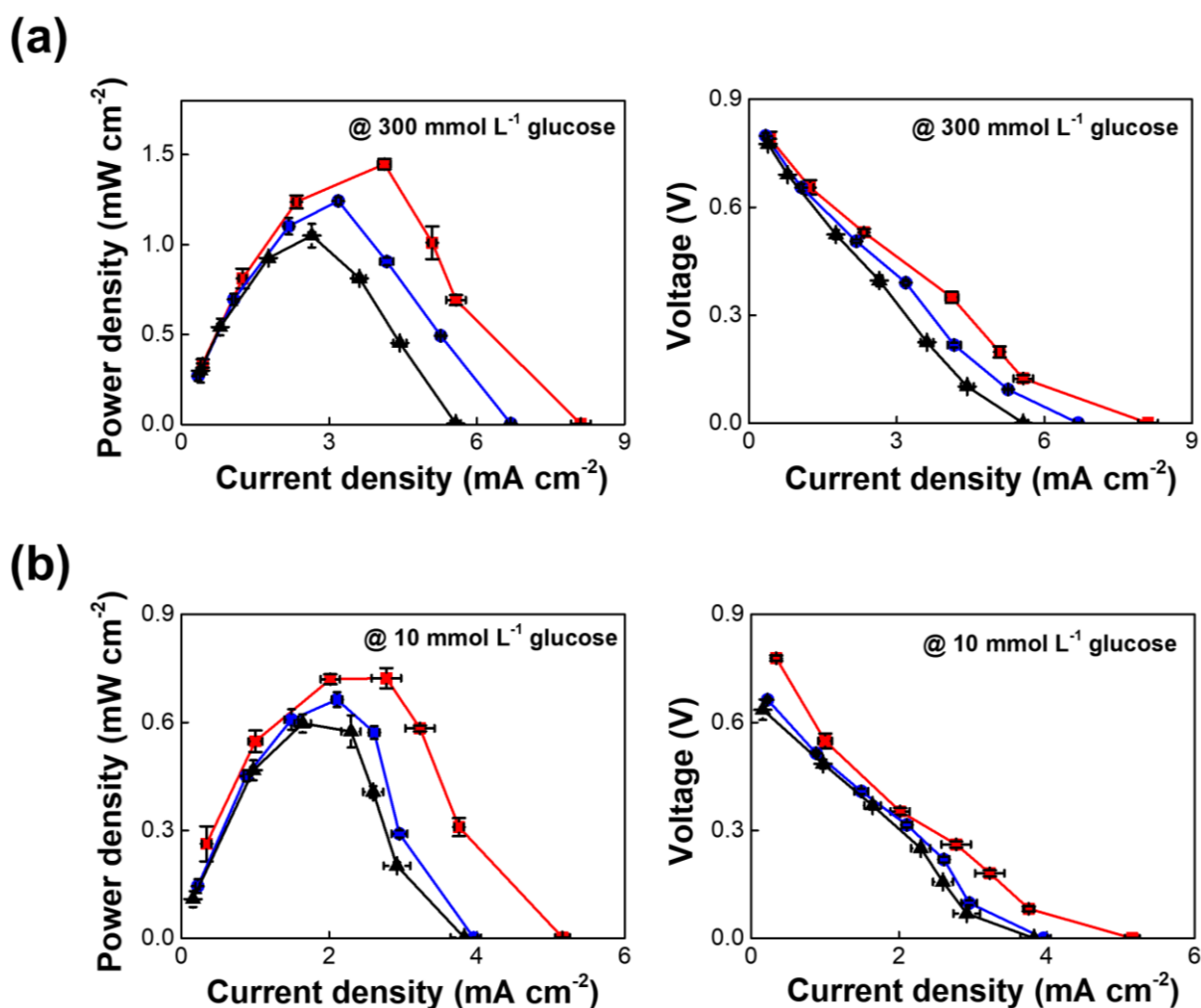
FIG. S42. External load-based power output profiles of BFCs. Power–current and voltage–current profiles of the complete BFCs with three different kinds of anodes in (a) 300 mmol L^{-1} and (b) 10 mmol L^{-1} glucose in PBS (at 36.5 °C). In this case, the anodes prepared from the (GOx/TOA-Au$_{NP}$)$_3$/MCT (red), the (GOx/DETA/C-Au$_{NP}$/DETA)$_4$/MCT (blue), and the (GOx/DETA)$_3$/MCT (black) were combined with the Pt-MCT cathode for the preparation of the complete BFCs.
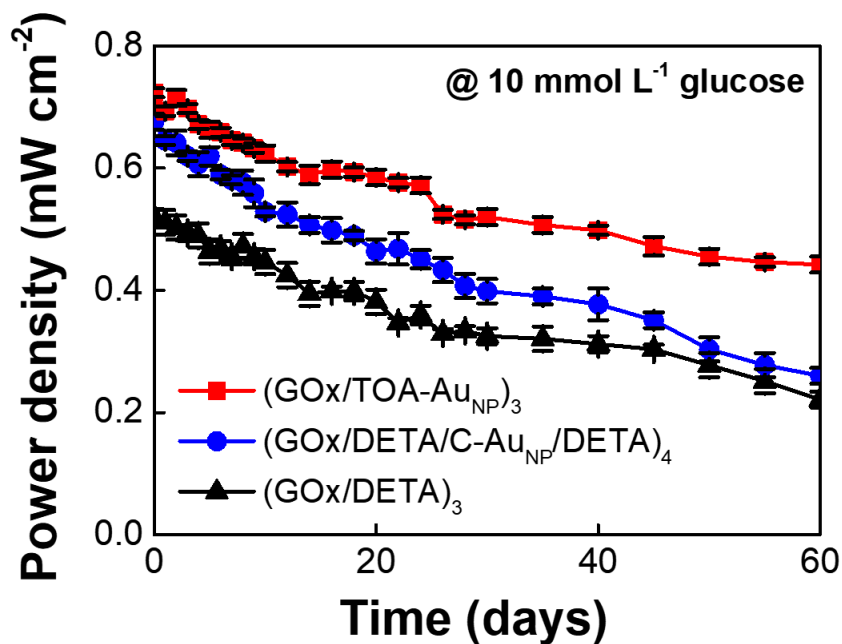
FIG. S43. Power density stability of BFCs. Power output stabilities of the complete BFCs prepared from three different kinds of anodes in 10 mmol L^{-1} glucose in PBS. For this investigation, continuous operation over 60 days was tested with external variable resistors. Additionally, the anodes used in this study were (GOx/TOA-Au$_{NP}$)$_3$/MCT (red), (GOx/DETA/C-Au$_{NP}$/DETA)$_4$/MCT (blue), and (GOx/DETA)$_3$/MCT (black). On the other hand, the cathode was fixed at Pt-MCT. In this case, glucose buffers were replaced daily for continuous operation.
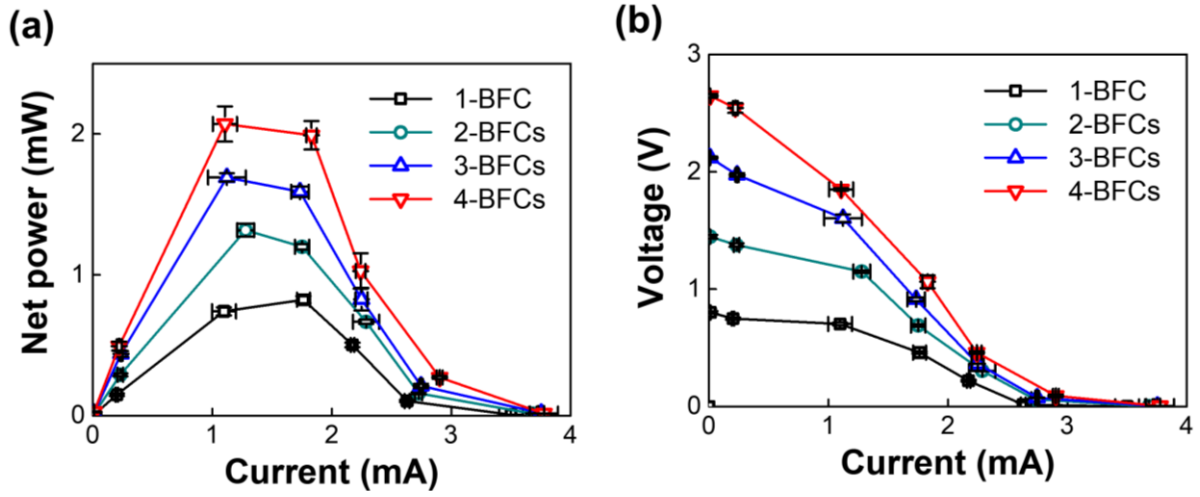
FIG. S44. Net power output profiles of BFCs. (a) Net power– current and (b) voltage–current profiles of four different series-connected BFCs with varying the external resistances from 1 kΩ to 1 GΩ.
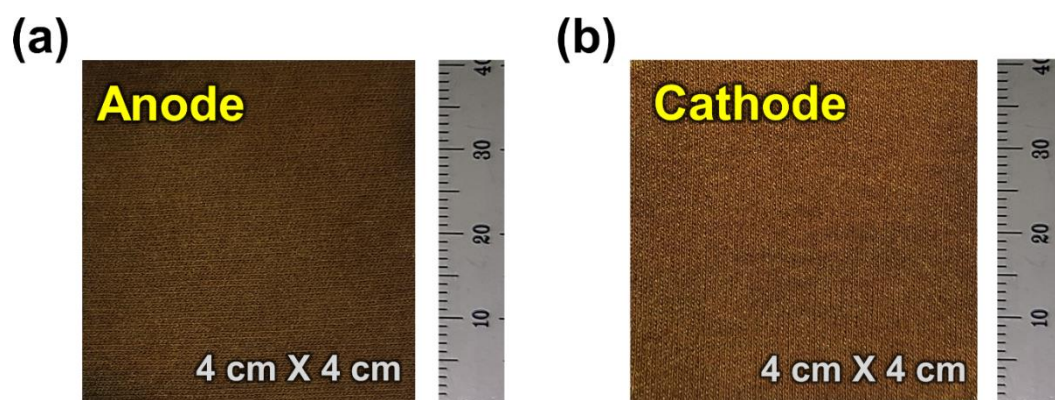
**FIG. S45.** BFC electrodes. Photographic images of a) large-sized BFC anode and b) cathode.
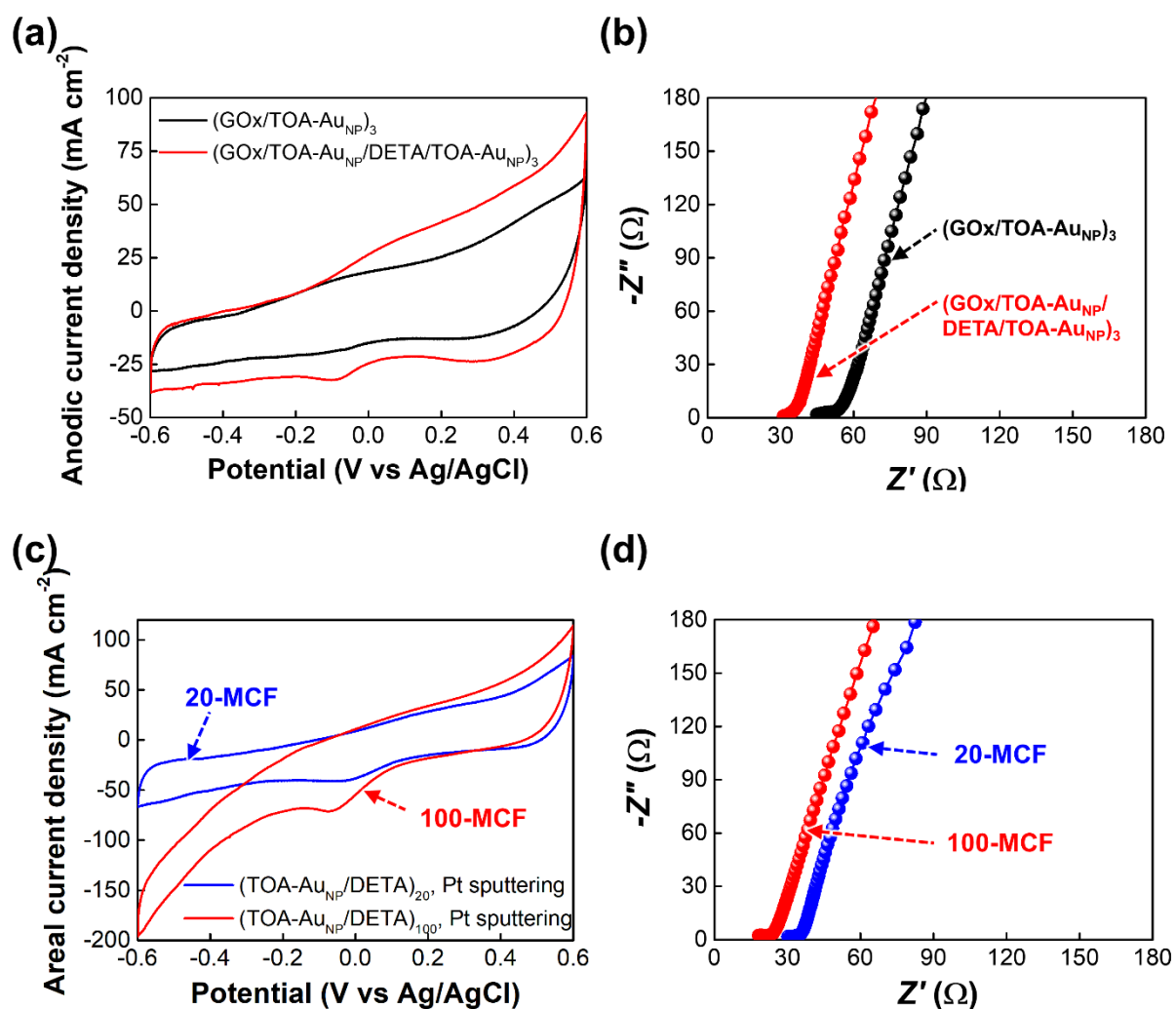
FIG. S46. Electrochemical performance of the MCF anodes and cathodes. (a) CVs of (GOx/TOA-Au$_{NP}$)$_3$/MCF (black) and (GOx/TOA-Au$_{NP}$/DETA/TOA-Au$_{NP}$)$_3$/MCF (red) anodes with the diameter of 200 μm, the length of 5.0-mm, and the active external surface area of 3.14 mm^2 measured at the potential range −0.6 to +0.6 V. (b) Nyquist plots tested in PBS with 300 mmol L^{-1} glucose solution. The electrochemical measurements of (a), (b) were performed in PBS with 300 mmol L^{-1} glucose at 36.5 °C under ambient conditions. (c) CVs of 20-MCF [i.e., Pt-sputtered (TOA-Au$_{NP}$/DETA)$_{20}$/MCF] (blue) and 100-MCF [i.e., Pt-sputtered (TOA-Au$_{NP}$/DETA)$_{100}$/MCF] (red) cathodes measured at the potential range −0.6 to +0.6 V. (d) Nyquist plots tested in PBS. The electrochemical measurements of (c), (d) were performed in PBS at 36.5 °C under ambient conditions.
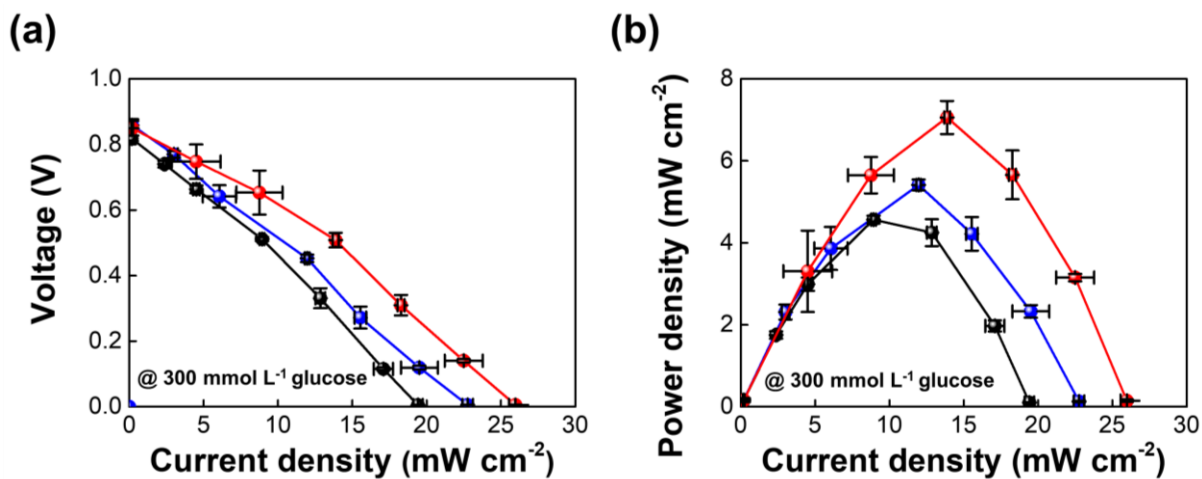
FIG. S47. External load-based power output profiles of MCF-BFC. (a) Power (P) – current (I) profile and (b) Voltage (V) – current (I) profiles of single MCF-BFCs of the complete BFCs: (GOx/TOA-Au$_{NP}$)$_3$/MCF//Pt-20-MCF (black), (GOx/TOA-Au$_{NP}$)$_3$/MCF//Pt-100-MCF (blue), and (GOx/TOA-Au$_{NP}$/DETA/TOA-Au$_{NP}$)$_3$/MCF//Pt-100-MCF (red). The power output was obtained in PBS solution containing 300 mmol L^{-1} glucose (under ambient conditions at 36.5 °C) by measuring the current flowing through external variable resistors (from 1 kΩ – 10 GΩ) to control the cell potential.
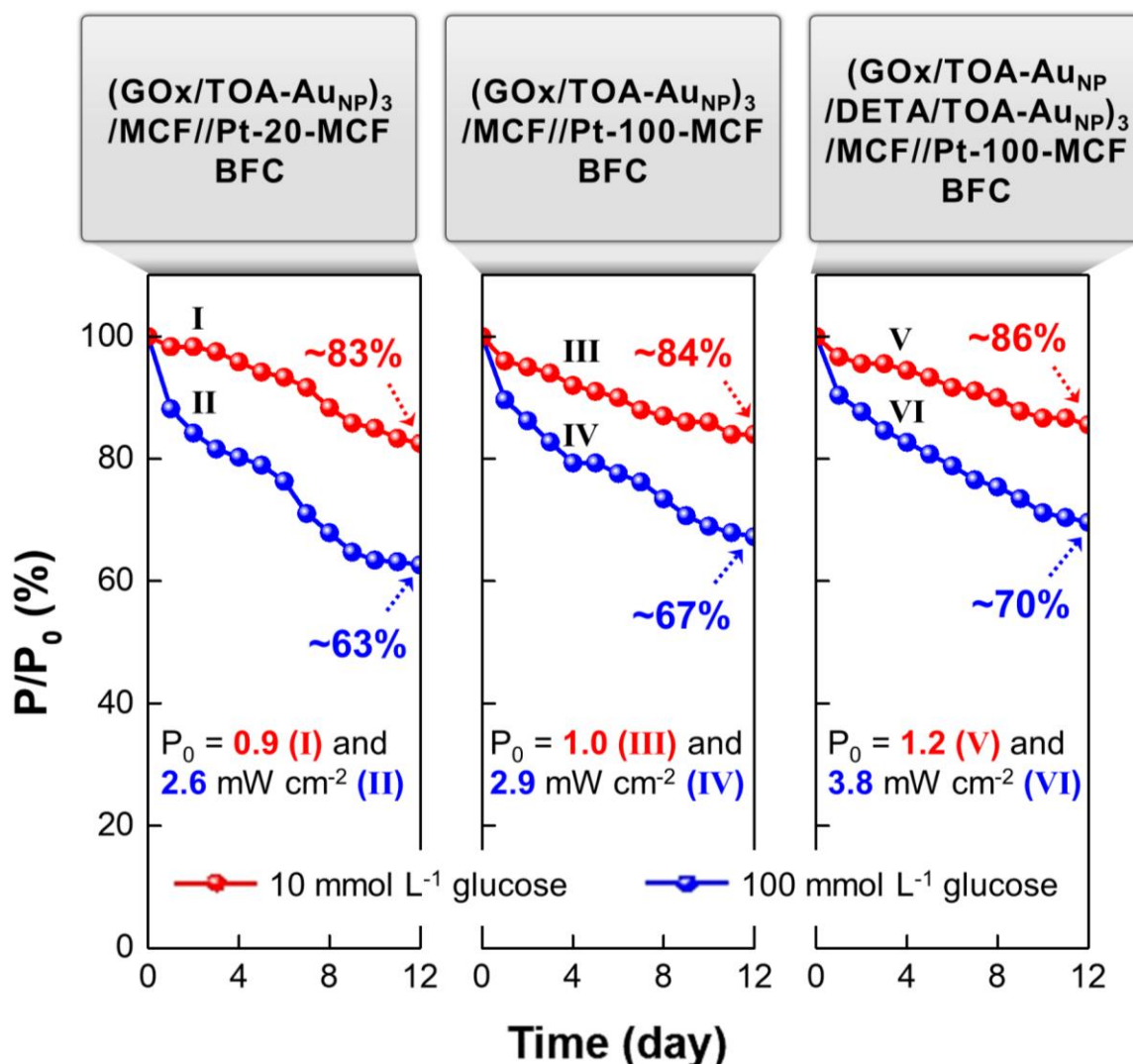
FIG. S48. Power density stability of MCF-BFCs. Power output stabilities of the complete BFCs in 10 mmol L^{-1} and 100 mmol L^{-1} glucose in PBS over 12 days with external variable resistors. I, II: (GOx/TOA-Au$_{NP}$)$_3$/MCF//Pt-20-MCF BFC [10 mmol L^{-1} (I), 100 mmol L^{-1} (II)]. III, IV: (GOx/TOA-Au$_{NP}$/DETA/TOA-Au$_{NP}$)$_3$/MCF//Pt-100-MCF BFC [10 mmol L^{-1} (III), 100 mmol L^{-1} (IV)]. V, VI: (GOx/TOA-Au$_{NP}$/DETA/TOA-Au$_{NP}$)$_3$/MCF//Pt-100-MCF BFC [10 mmol L^{-1} (V), 100 mmol L^{-1} (VI)]. In these cases, glucose buffers were replaced daily for continuous operation. Each initial power densities (P_0) were 0.9 (I), and 2.6 (II), 1.0 (III), 2.9 (IV), 1.2 (V), and 3.8 mW cm^{-2} (VI).

Table S1. Power output performance of various textile-type BFCs reported to date.

BFC electrode	Catalysts[a] Anode// Cathode	Areal P_{max} (mW cm^{-2})	Net P_{max} (mW)	Stability	ET[b] (method)	Ref.
MCT[c]	(GOx/Au$_{NP}$) //Pt-sputtered (TOA-Au$_{NP}$/DETA)	1.5	2.1 (4-BFCs)	81% after 20 days (61% after 60 days)	DET (using R_{ext})	Our work
Gore-Tex textile	LOx + Pt //Lac	0.07	0.0126[d]	~50% after 4 weeks	MET (using CV)	S9
Garments (headbands or wristbands)	GOx //BOD	0.1	0.0045[d]	~80% after 6 h	MET (using CV)	S10
Pantyhose textile	FDH //BOD	0.2	0.2[e]	62% remained after 30cycles of 50% stretching	MET (using R_{ext})	S11
Nylon–spandex textile	FDH //BOD	0.25	-	-	MET (using CV)	S12
Polyurethane sheet	GOx //BOD	0.125	0.025[d]	-	MET (using R_{ext})	S13
Wearable wristband	LOx//Ag$_2$O	0.25	0.23[d]	-	MET (using CV)	S14
Cotton textile cloth	LOx/Pt//BOD	0.216	0.38 (4-BFCs)	~90% after 72 h	MET (using R_{ext})	S15
CNT-modified carbon fabric	FDH//BOD	0.95	0.64 (3-BFCs)	-	DET (using R_{ext})	S16

[a] The abbreviations for different enzymes: lactate oxidase (LOx), laccase (Lac), bilirubin oxidase (BOD), and fructose dehydrogenase (FDH)

[b] ET: electron transfer mechanisms, DET: direct electron transfer. MET: mediated electron transfer, R_{ext}: external circuit resistance, and CV: cyclic voltammetry)

[c] MCT: metallic cotton textile

[d] Each value was calculated by the reported surface area of the BFC electrode.

Table S2. Power output performance of various fiber-type BFCs reported to date.

Host electrode	Areal P_{max} (mW cm^{-2})	OCV (V)	ET[a] (method)	Ref.
MCF[b]	7.3	0.82	DET (using R_{ext})	Our work
CNT fiber	0.74	0.83	MET (using R_{ext})	S17
	1.2	0.85	DET (using R_{ext})	S18
	0.74	0.6	MET (using R_{ext})	S19
	0.2	0.4	MET (using R_{ext})	S20
CNT/rubber fiber	0.04	0.58	MET (using R_{ext})	S21
CNT yarn	2.18	0.7	MET (using R_{ext})	S22
Cotton fiber	3.7	0.85	DET (using R_{ext})	S23

[a] ET: electron transfer mechanisms, DET: direct electron transfer. MET: mediated electron transfer, R_{ext}: external circuit resistance

[b] MCF: metallic cotton fiber

Supplementary References

[S1]Y. Ko, H. Baek, Y. Kim, M. Yoon, J. Cho, ACS Nano **7**(1), 143 (2013).

[S2]K. Zhou, Y. Zhu, X. Yang, C Li, Electroanalysis **22**(3), 259 (2010).

[S3]Q. Wang, X. Zhang, L. Huang, Z. Zhang, S. Dong, Angew. Chem. Int. Ed. **56**(50), 16082 (2017).

[S4]M. Portaccio, B. Della Ventura, D. G. Mita, N. Manolova, O. Stoilova, I. Rashkov, M. Lepore, J. Sol-Gel Sci. Technol. **57**(2), 204 (2011).

[S5]S. Wu, H. X. Ju, Y. Liu, Adv. Funct. Mater. **17**(4), 585 (2007).

[S6]S.-J. Bao, C. M. Li, J.-F. Zang, X.-Q. Cui, Yan Qiao, J. Guo, Adv. Funct. Mat. **18**(4), 591 (2008).

[S7]M. Zhao, Y. Gao, J. Sun, F. Gao, Anal. Chem. **87**(5), 2615 (2015).

[S8]H. J. Hecht, H. M. Kalisz, J. Hendle, R. D. Schmid, D. Schomburg, J. Mol. Biol. **229**(1), 153 (1993).

[S9]W. Jia, G. Valdés-Ramírez, A. J. Bandodkar, J. R. Windmiller, J. Wang, Angew. Chem. Int. Ed. **52**(28), 7233 (2013).

[S10]W. Jia, X. Wang, S. Imani, A. J. Bandodkar, J. Ramírez, P. P. Mercier, J. Wang, J. Mater. Chem. A **2**(43), 18184 (2014).

[S11]Y. Ogawa, Y. Takai, Y. Kato, H. Kai, T. Miyake, M. Nishizawa, Biosens. Bioelectron. **74**, 947 (2015).

[S12]I. Jeerapan, J. R. Sempionatto, A. Pavinatto, J.-M. You, J. Wang, J. Mater. Chem. A **4**(47), 18342 (2016).

[S13]A. J. Bandodkar, I. Jeerapan, J.-M. You, R. Nuñez-Flores, J. Wang, Nano Lett. **16**(1), 721

(2016).

[S14]J. Lv, I. Jeerapan, F. Tehrani, L. Yin, C. A. Silva-Lopez, J.-H. Jang, D. Joshuia, R. Shah, Y. Liang, L. Xie, F. Soto, C. Chen, E. Karshalev, C. Kong, Z. Yang, J. Wang, Energy Environ. Sci. **11**(12), 3431 (2018).

[S15]S. Yin, Z. Jin, T. Miyake, Biosens. Bioelectron. **141**, 111471 (2019).

[S16]T. Miyake, K. Haneda, S. Yoshino, M. Nishizawa, Biosens. Bioelectron. **40**(1), 45 (2013).

[S17]F. Gao, L. Viry, M. Maugey, P. Poulin, N. Mano, Nat. Commun. **1**, 2 (2011).

[S18]C. H. Kwon, Y. Ko, D. Shin, S. W. Lee, J. Cho, J. Mater. Chem. A **7**(22), 13495 (2019).

[S19]S. Yin, X. Liu, T. Kaji, Y. Nishina, T. Miyake, Biosens. Bioelectron. **179**, 113107 (2021).

[S20]F. C. P. F. Sales, R. M. Iost, M. V. A. Martins, M. C. Almeida, F. N. Crespilho, Lab Chip **13**(3), 468 (2013).

[S21]H. J. Sim, D. Y. Lee, H. Kim, Y.-B. Choi, H.-H. Kim, R. H. Baughman, S. J. Kim, Nano Lett. **18**(8), 5272 (2018).

[S22]C. H. Kwon, S.-H. Lee, Y.-B. Choi, J. A. Lee, S. H. Kim, H.-H. Kim, G. M. Spinks, G. G. Wallace, M. D. Lima, M. E. Kozlov, R. H. Baughman, S. J. Kim, Nat. Commun. **5**, 3928 (2014).

[S23]C. H. Kwon, Y. Ko, D. Shin, M. Kwon, J. Park, W. K. Bae, S. W. Lee, J. Cho, Nat. Commun. **9**(1), 4479 (2018).